FINAL NEER REPORT

(**DE-FG07-02ID14338)**

Project Title: **The Effect of Localized Flow on Fracture of Reactor Components**

Covering Period: June 01, 2003 – Dec. 31, 2008

Date of Report: Dec. 21, 2008

Recipient: **University of Missouri-Rolla** (Now Missouri University of Science & Technology)

Award Number: **DE-FG07-02ID14338**

Subcontractors: None

Other Partners: None

Contract(s): Arvind S. Kumar, (573) 341-4747, kumar@mst.edu

Project Objective: Finite Element Analysis of Plastic Deformation and Fracture in Reactor Components

Background and Status: Final Report

Plans for Next Year: Final Report.

FINAL NEER REPORT

(DE-FG07-02ID14338)

The Effect of Localized Flow on Fracture of Reactor Components

By

Arvind S. Kumar, PI

Graduate Student – Michael Lampe

Missouri University of Science & Technology

(Formerly University of Missouri-Rolla)

Submitted to :

U.S. Depart of Energy

Dec. 21, 2008

ABSTRACT

The effect of flow localization on plastic flow and fracture due to stress concentrations in type 316 stainless steel was studied by dynamic finite element modeling (FEM) using a computer code (ABAQUS Explicit). It was found that the presence of cracks is responsible for a sharp decrease in fracture energy of specimens. The dependence of fracture energy on crack depth is exponential. For round specimens with no cracks, the fracture energy is directly proportional to cross-sectional area. Fracture energy is relatively independent of crack opening angle (<140 degrees) due to the fact that as soon as the crack tip propagates the tip is blunted making the effect of the original stress concentration at the crack tip irrelevant.

The fracture energy dependence on circumferential crack depth, crack opening, and sharpness of the crack tip can be explained by examining the fracture energy density profiles around the crack tip, as determined by finite element modeling (FEM). For benchmarking purposes, the ABAQUS Explicit, with the user supplied subroutine, calculated fracture energy was made equal to the experimental value of fracture energy of both unirradiated and irradiated specimens. FEM of specimens containing cracks of different depths, angles, and crack tip sharpness is performed for round specimens to obtain the respective fracture energies and the energy distribution along the gauge length of various specimens.

Irradiated specimens behaved similar to the unirradiated specimens. However, the irradiated specimen fracture energy is less sensitive to the notch root radius than the unirradiated specimen. One explanation is that the ratio of the global and local stress, strain, and absorbed energy is less for the irradiated specimen than that of the unirradiated specimen.

1. INTRODUCTION

Most reactor components and structural members are made from alloys due to their ability to resist brittle fracture. However, brittle fracture can occur when the structural member cannot undergo extensive plastic deformation throughout the structure due to flow localization in small volumes, resulting from stress concentrators (e.g. a sharp notch) or the presence of dislocation channels. This process is referred to as flow localization or plastic instability. This process results in a fracture mode that appears to be brittle since only small volumes of the material are able to deform through plastic flow. Even though there is extensive plastic flow in the small, confined regions, deformation essentially results in brittle fracture since very little energy is required to induce fracture. This study will examine the effect of plastic flow localization on fracture energy due to various types of stress concentrators on embrittlement.

From a typical tension test, an engineering stress – strain curve can be created from load – displacement data. Figure 1.1 shows an example of an engineering stress – strain curve. The curve can be split into 3 stages. In stage 1 the tension specimen deforms elastically. The first and second stages are divided by the yield stress, which in this case was determined using the 0.2% offset method. In stage 2, the specimen plastically deforms, and is strain hardened. The second and third stages are divided by the ultimate tensile stress (UTS). In the third stage, the specimen undergoes plastic instability.

When the specimen reaches UTS, the work hardening rate falls, and the volume around stress concentrations in the specimen become more susceptible to fracture. The elevated local stress accelerates the local strain, and concentrates the stress at stress concentrators resulting in the formation of a “neck” in the specimen where the specimen fractures shortly thereafter.

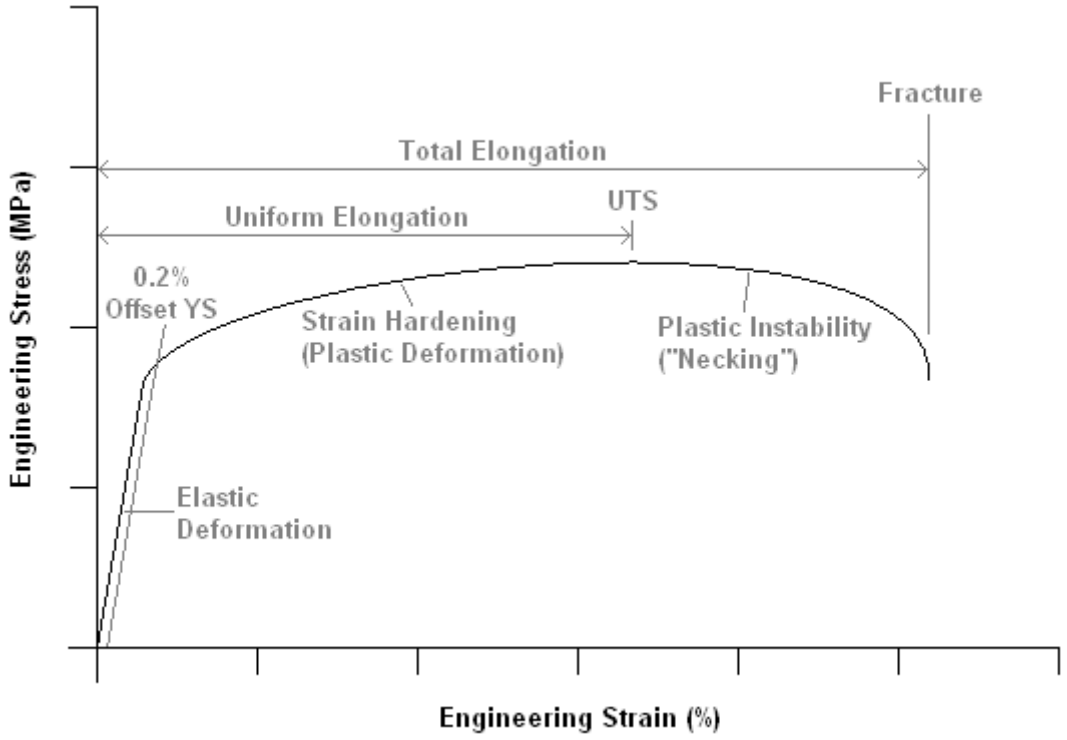

Figure 1.1. Example Engineering Stress – Strain Curve

Tension tests can be used to investigate the relationship between ductility and stress concentrators [1]. Such stress concentrators may be present in all structures, including nuclear power plant structures such as baffle former plates and baffle former bolts in pressurized water reactors. In French reactors, the baffle former bolts have fractured at the connection of the bolt head and the bolt shank [2] which is itself a stress concentrator.

After fast neutron irradiation, the yield stress increases and the strain to fracture is reduced. The UTS also increases but not as much as the yield stress. Figure 1.2 shows the effects of irradiation on stainless steel 316.

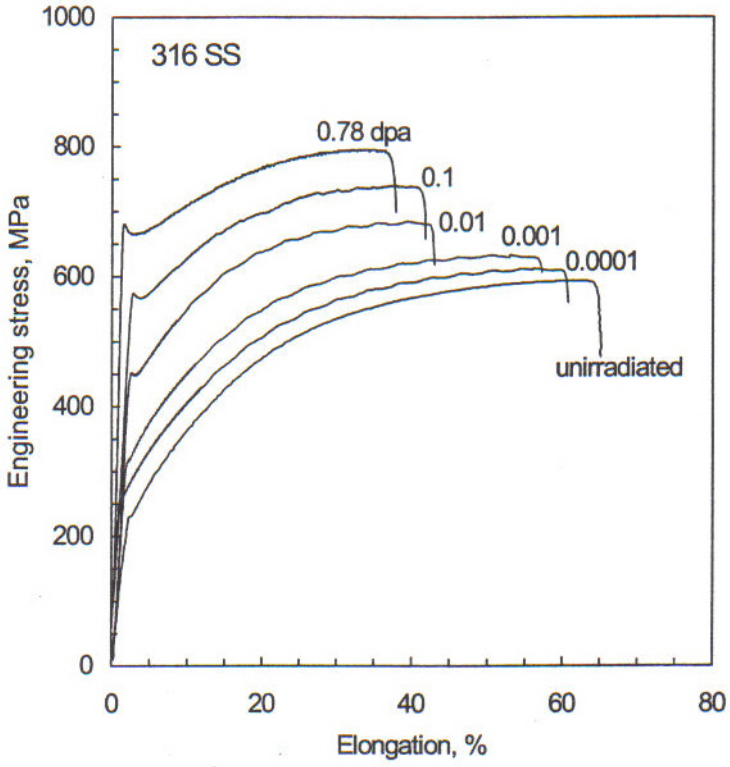

Figure 1.2. Effects of Irradiation on 316 SS [3]

As irradiation dose (dpa) increases there appears to be the development of a yield drop. The yield stress increase is the result of microstructural defects pinning dislocations and preventing their glide. Once the upper yield stress is reached the dislocations can dislodge from pinning defects and plastic deformation can occur at a lower yield stress.

2. REVIEW OF LITERATURE

It is important to understand the microstructural behavior of the material of interest during a tension test. The material chosen for this study is type 316 stainless steel (316 SS). This material is used in many pressurized water reactors for the baffle-former plates and bolts. The major contributors to the cracking of plates and bolts are the number of major power transients, differential thermal expansion and neutron fluence [2].

Fish [4] has studied notch effects on tensile behavior since 1976. His work examined the effects of V- and C- notches 0.0762 cm (0.030 in.) deep in a flat specimen with a thickness of 0.1016 cm (0.040 in.) and gauge length of 0.3175 cm (0.125 in.). He investigated the effects of notches on the ultimate tensile strength (UTS) at two different levels of neutron fluence. At a low strain rate the V- and C-notches resulted in the same UTS which was lower than that of the unnotched specimen. At a high strain rate, the C-notched specimen had greater UTS than the V-notch specimens. No noticeable difference was seen between specimens irradiated at about 5.5 x 10^22 n/cm^2 and 9.5 x 10^22 n/cm^2 with neutron energy greater than 0.1 MeV.

To complement the experimental techniques mentioned earlier, a finite element modeling (FEM) code (ABAQUS Explicit) has been successfully used by Sidener [5], Kumar [6], and McCoy [7, 8, 9].to examine the fracture behavior of steel specimens of different sizes and to predict the fracture energy of larger specimens based on the experimentally determined fracture energy of smaller specimens. FEM has the advantage of evaluating the fracture performance of specimens of various sizes and notch geometry based on tensile data obtained in uniaxial tests resulting in considerable savings of time and expense when compared with the neutron irradiation and testing of each specimen of interest.

Kim [10] has used ABAQUS to study plastic deformation in notched bars and plates in tension. Axisymetry was used to simulate the notched bar, while the notched plate used plane strain elements in a 2D model. The geometry is divided into small regions where the computer code calculates the distribution of stress and strain. This division is referred to as a mesh. The meshing near the notches was refined while meshing away from the notches was coarse.

Wu has used a combination of ABAQUS standard and physical tension testing to study notch strengthening [11]. Four specimens were studied, 2 V-notch and 2 C-notch round specimens with 0.8 cm diameters. For each type, one notch had a small depth, with a depth to diameter ratio of 0.129, while the other had a larger depth with a ratio of 0.214. The sharper and deeper notches were more effective in localizing the plastic deformation. The presence of notches and neutron irradiation facilitated a transition from ductile to brittle failure.

The present work will further examine the notch effects on fracture energy for both unirradiated and irradiated 316 SS. For both V-notch and C-notch geometries, the effect of notch depth and notch angle on fracture energy will be investigated.

3. ABAQUS METHODOLOGIES

Modeling of the tensile specimens was preformed using ABAQUS Explicit, an explicit dynamic finite element code, from Simulia [12-14]. Most input files were created using ABAQUS CAE version 6.6 [13]. Some input files were generated by renaming already existing input files and changing the material properties by hand.

A simplified explicit dynamic algorithm is presented to explain the calculations that the finite element code uses. Each calculation takes place over a given time increment. At the beginning of the time increment, time t, there is dynamic equilibrium at each node which is simply the sum of the forces, on the node being equal to the mass, multiplied by the nodal acceleration.

Equation 3.1. Forces Acting on a Node

$$\sum F = M \cdot \ddot{u}$$

The forces acting on the node are an externally applied force vector (F_E) and internal element force vector (F_I). The nodal acceleration for increment number i, is solved for by dividing the forces by the mass matrix.

Equation 3.2. Nodal Acceleration

$$\ddot{u}_i = \frac{(F_E - F_I)_i}{M}$$

ABAQUS Explicit uses an explicit central difference time-integration rule to solve for the nodal velocities and displacements. Knowing the mean velocity from the previous increment (i-1/2) and the acceleration for increment number i, the mean velocity of the node for the next increment (i+1/2) can be solved for. The mean velocity of the previous increment

is added to the average time of increments i and i+1, multiplied by the acceleration at increment i.

Equation 3.3. Nodal Mean Velocity

$$\dot{u}_{i+1/2} = \dot{u}_{i-1/2} + \frac{(\Delta t_{i+1} + \Delta t_i)}{2} \ddot{u}_i$$

Using the mean velocity from above the displacement at the end of the time increment is determined:

Equation 3.4. Nodal Displacement

$$u_{i+1} = u_i + \Delta t_{i+1} \cdot \dot{u}_{i+1/2}$$

The nodal calculation of acceleration required the internal element forces, or force vectors. The elemental calculations that determine the internal element forces require the stresses, σ, and state variables, V_s, of that element. Theses variables can be determined using the following constitutive equations.

Equation 3.5. Stress Constitutive Equation

$$\sigma_{i+1} = f(\sigma_i, V_{s,i}, \Delta\varepsilon)$$

Equation 3.6. State Variable Constitutive Equation

$$V_{s,i+1} = g(\sigma_i, V_{s,i}, \Delta\varepsilon)$$

Once all calculations for increment i+1 are complete, increment i+1 becomes increment i and the algorithm starts over for the next time increment.

The size of a time increment is, by default, automatically determined by ABAQUS/Explicit to ensure that the central difference time integration is stable. This is

accomplished by determining the dilatational wave speed, C_d, and characteristic dimension, L, on an element-by-element basis, as seen below:

Equation 3.7. Stable Time Increment Size

$$\Delta t_{stable} = \min\left(\frac{L}{C_d}\right)$$

The dilatational wave speed is calculated using Lame's constants, λ and μ, and density, ρ, which are all material properties.

Equation 3.8. Dilatational Wave Speed

$$C_d = \sqrt{\frac{\lambda + 2\mu}{\rho}}$$

Thus, material properties affect the dilatational wave speed. It is important to note that Lame's constants, and consequently the dilatational wave speed, change as the material undergoes non-linear deformation. Even with this in mind, the dilatational wave speed is proportional to the inverse of the square root density.

Equation 3.9. Dilatational Wave Speed Proportionality

$$C_d \propto \frac{1}{\sqrt{\rho}}$$

The stable time increment can then be rewritten as proportional to the square root density multiplied by the characteristic length.

Equation 3.10. Stable Time Increment Size Proportionality

$$\Delta t_{stable} \propto L \cdot \sqrt{\rho}$$

It is important because the element-by-element estimation will give a smaller time increment than the actual stability limitation of the whole model. With this in mind, one can artificially decrease the time increment by increasing the mass, which would increase the density. This is referred to as "mass scaling" [12]. When using such a technique, the mass must not be increased so much that the time increment would exceed the actual stability limitation.

In cases were mass scaling interfere with the calculation, the solution could diverge and result in an error and the end of the simulation. It is also possible for the simulation to run to completion with erroneous results which can easily be identified by examining the resulting energies. The "artificial" strain energy must be negligible compared to the "real" energies, such as external work (ALLWK) [12]. The external work and internal energy (ALLIE), or total strain energy, must also be approximately equal. Both of these requirements must be met for the solution to be considered valid.

The time it takes for ABAQUS/Explicit to run a job can be estimated by:

Equation 3.11. Computational Time

$$T_{CPU} \approx N \frac{T_{Event}}{\Delta t_{stable}}$$

The time it takes for the computer to run an ABAQUS/Explicit job to completion is T_{CPU}. N is the total number of elements present in the model. T_{Event} is the duration of the event under examination in ABAQUS Explicit. Looking at the equation above, it is easy to see that as the stable time increment increases, the overall CPU time decreases. Also as the mesh is refined, having more elements in the same size part, the CPU time increases since the

total number of elements increase and because the stable time increment decreases as a result of a decreasing characteristic length.

4. FAILURE CRITERIA

This section discusses the ABAQUS Explicit failure criteria, along with user subroutines, for accurately modeling the failure of a stainless steel 316 low carbon tensile specimen in a tensile test. Scott Sidener's subroutine was used for multiple publications [5 and 6], and is examined and explained in this section. An improved version of his subroutine was developed to better model the failure of the stainless steel. It is similar in concept to Dr. Jamie McCoy's Multi-Hardening Modulus subroutine [15].

4.1 ABAQUS FAILURE CRITERIA

ABAQUS has multiple options for modeling the failure of elastic-plastic material. The most suitable option is the ductile initiation criteria for starting the crack and the damage evolution and elemental removal for the crack propagation.

In the ductile initiation model, the equivalent plastic strain at the onset of damage (ε_D^{pl}) is assumed to be a function of stress triaxiality (η) and equivalent plastic strain rate ($\dot{\varepsilon}^{pl}$). This function is an empirical correlation owned by Simulia, which owns ABAQUS, and is not revealed in the literature. Stress triaxiality is a function of pressure stress (p)and the von Mises equivalent stress (q). The equivalent plastic strain, stress triaxiality, pressure stress, and von Mises equivalent stress are defined in the equations below [12].

Equation 4.1. Equivalent Plastic Strain [12]

$$\varepsilon_D^{pl} = f\left(\eta, \dot{\varepsilon}^{pl}\right)$$

Equation 4.2. Stress Triaxiality [12]

$$\eta = -\frac{p}{q}$$

Equation 4.3. Pressure Stress [12]

$$p = -\frac{1}{3}\left(\sigma_{11} + \sigma_{22} + \sigma_{33}\right)$$

where:

σ_{11} = principal stress in direction 1

σ_{22} = principal stress in direction 2

σ_{33} = principal stress in direction 3

Equation 4.4. von Mises Equivalent Stress [6]

$$q = \sqrt{\frac{1}{2}\left[\left(\sigma_{11} - \sigma_{22}\right)^2 + \left(\sigma_{22} - \sigma_{33}\right)^2 + \left(\sigma_{33} - \sigma_{11}\right)^2 + 3\left(\sigma_{12}^2 + \sigma_{23}^2 + \sigma_{31}^2\right)\right]}$$

where:

σ_{12}, σ_{23}, and σ_{31} are shear stresses in their respective directions

For each increment the equivalent plastic strain is determined at each integration point, which is the point or points where elemental calculations take place. The equivalent plastic strain is compared to the equivalent plastic strain at the onset of damage for each increment, as seen in the equation below:

Equation 4.5. Incremental State Variable for the Ductile Damage Initiation [12]

$$\Delta\omega_D = \frac{\Delta\varepsilon^{pl}}{\varepsilon_D^{pl}\left(\eta, \dot{\varepsilon^{pl}}\right)} \geq 0$$

where:

$\Delta\varepsilon^{pl}$ = equivalent plastic strain over an increment

$\Delta\omega_D$ = state variable over an increment

The incremental state variable is added to the previous increment's state variable. When the summation of the incremental state variable reaches one, damage is initiated.

Equation 4.6. Ductile Damage Initiation Criteria [12]

$$\sum \Delta\omega_D = 1$$

Once damage is initiated it affects both the stress and the elasticity of the element. They are multiplied by a factor (1 – D) where D is the damage. Damage, D, is dependent on the chosen damage evolution method. In ABAQUS Explicit this method can be determined by equivalent plastic displacement or fracture energy [12]. D increases via damage evolution until it reaches D_{max}, the maximum damage, at an integration point, that point is failed. When all integration points in an element fail, the element is removed. The default value of D_{max} for most elements is 0.99 or 1.0. Figure 4.1 illustrates this process. Elastic deformation occurs until the yield stress () is met. The material plastically deforms until damage is initiated at the equivalent plastic strain (ε_D^{pl}) and the stress at the onset of damage (σ_D). D according to damage evolution and as a result the stress and elasticity are degraded. In this case when D reaches D_{max} of 1 the integration point has failed at reached the equivalent fracture strain (ε_f^{pl}).

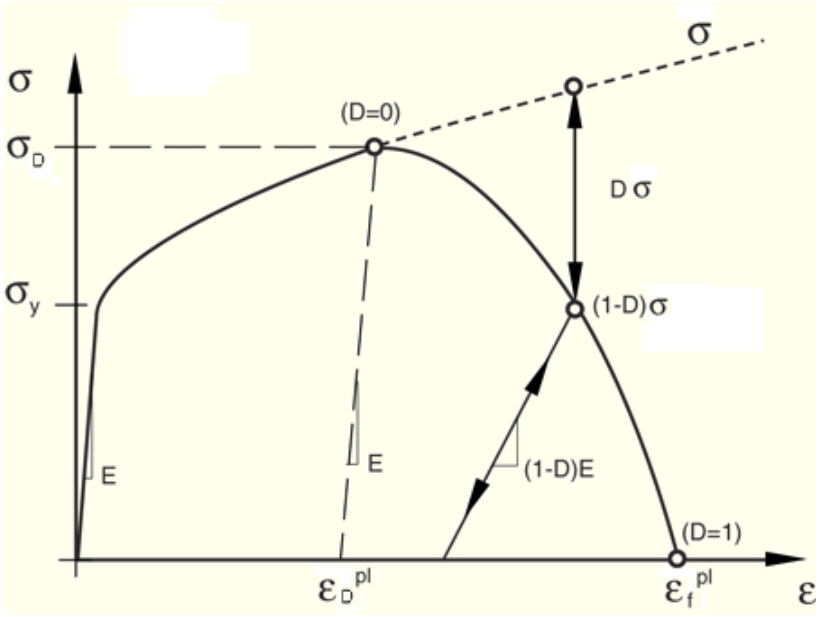

Figure 4.1. ABAQUS Ductile Damage Initiation and Evolution Example [12]

In order to use the Ductile Damage Initiation Criteria one must know the stress triaxiality and equivalent plastic strain rate that corresponds to the equivalent plastic strain at the onset of damage. These variables are not readily available for stainless steel 316L.

4.2 USER DEFINED METHODS

Scott Sidener developed a user-defined method using a FORTRAN subroutine, which is used instead of the ABAQUS failure method. Sidener's subroutine simplifies the initiation of a crack by only looking at a damage initiation plastic strain, defined by the user. This is similar to the equivalent plastic strain at the onset of damage in that once the plastic strain reaches the damage initiation plastic strain, damage is initiated. Knowledge of stress triaxiality is unnecessary with this subroutine.

The stress-strain curve is simplified to be bilinear. The first linear portion represents the elastic region of the curve, while the second linear portion is representative of the plastic deformation. The slope of the plastic deformation linearity is the strain hardening modulus, which is user defined. Once damage is initiated, the damage begins to increase, or evolve.

The damage evolution is assumed to be linear. The stress is degraded when once the damage initiation plastic strain is reached. Then the stress follows a straight line to the failure strain. Once the failure strain is reached the integration point is considered failed. Once all integration points are failed in an element, the element is deleted.

Another uniqueness Sidener's subroutine has over the ABAQUS Explicit model is that it only advances the damage of the stress and elasticity when the integration points experience tension. This is ensured by the use of an average stress (σ_{avg}) that needs to be

positive in order for the damage to occur (Equation 4.7). This is important because compressive loading would not cause damage in a metal.

Equation 4.7. Average Stress

$$\sigma_{avg} = \frac{1}{3}\left(\sigma_{11} + \sigma_{22} + \sigma_{33}\right)$$

To improve the accuracy of the user subroutine, this researcher, used Sidener's subroutine as a basis for a multi-linear hardening modulus (MLHM) method. The new subroutine uses the yield stress to initiate the plastic deformation, which is described by the use of the hardening modulus, just like Sidener's. However, the user also includes two plastic strains at which two other hardening modulus values would be used.

4.3 BENCHMARKING THE METHODS

A simple model was created and used to benchmark the new user subroutine to the Sidener subroutine and ABAQUS Explicit. The two user subroutines will be compared to the representative experimental plasticity which is entered into ABAQUS Explicit as a multitude of discrete points. Comparison of the results ends at the ultimate tensile strength, where degradation begins.

The model is made of 80 3D elements forming a square bar of 2 x 2 x 20 elements. Each element was a perfect cube with each side 1 cm long. A velocity of 0.5 cm/s was applied to both ends moving away from the center of the bar, creating tension, see Figure 4.2. The ABAQUS plastic model was given tabular data in Table 4.1 which approximates the annealed 316 stainless steel at 50°C using experimental data. Sidener's subroutine uses the UTS stress and plastic strain as the point of initiating the degradation. The hardening modulus is the slope of the line created by connecting the yield stress and the UTS. The new

subroutine uses 3 hardening modulus values to better approximate the plastic deformation. It also uses the UTS as the initiation point for degradation. Both subroutines used a fracture strain that was 0.1 beyond the strain at UTS. All three methods used a density of 7.99 g/cm^3. Figure 4.3 shows the stress strain curves used by ABAQUS, Siderner's subroutine and the new subroutine.

Table 4.1. ABAQUS Explicit Plasticity for Benchmarking User Subroutines

True Stress (MPa)	Plastic Strain (cm/cm)
284	0.00000
348	0.01913
392	0.03895
463	0.07832
525	0.11665
582	0.15393
636	0.19095
684	0.22521
729	0.25921
770	0.29232
807	0.32449
841	0.35577
871	0.38612
899	0.41565
990	0.51563
1197	0.74653
1417	0.99653
1635	1.24653
2285	1.99653
3149	2.99653

The multi-linear hardening modulus model (new subroutine) compared better to the ABAQUS tabular data than the single-linear hardening model (Sidener's subroutine). First, the external work on the specimen was examined. As seen in Figure 4.4, the MLHM follows the ABAQUS plasticity closer than the SLHM. Once damage is initiated the failure models no longer follow the same trend of the ABAQUS plasticity. Shortly after damage initiation, the specimen breaks and the external work plateaus. Both failure models preformed as expected.

There is a greater difference in the models regarding the resulting stresses in the elements. Figure 4.5 shows the stress component 33, which is stress in the direction of tension, versus time. The MLHM model clearly outperformed the SLHM model. The MLHM model closely follows the ABAQUS plasticity model, while the SLHM model starts with under predicting the stress then switching over to predicting the stress before reaching damage initiation. Given the input stress strain curves for the models (Figure 4.3), the resulting performance of the models was expected.

There is a slight increase in runtime for the MLHM model, but otherwise it out performs the SLHM model. The MLHM was used instead of its predecessor for the studies presented and discussed in sections 6 and 7. A copy of the ABAQUS Explicit input for use with the MLHM user subroutine is located in Appendix A.

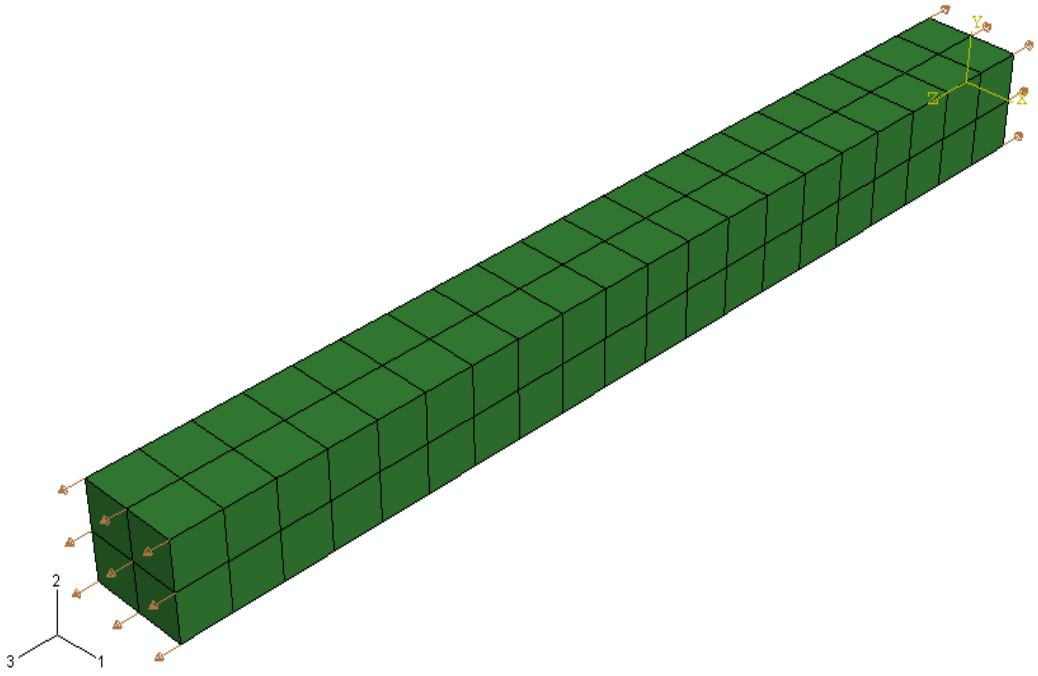

Figure 4.2. ABAQUS Explicit Benchmarking Model

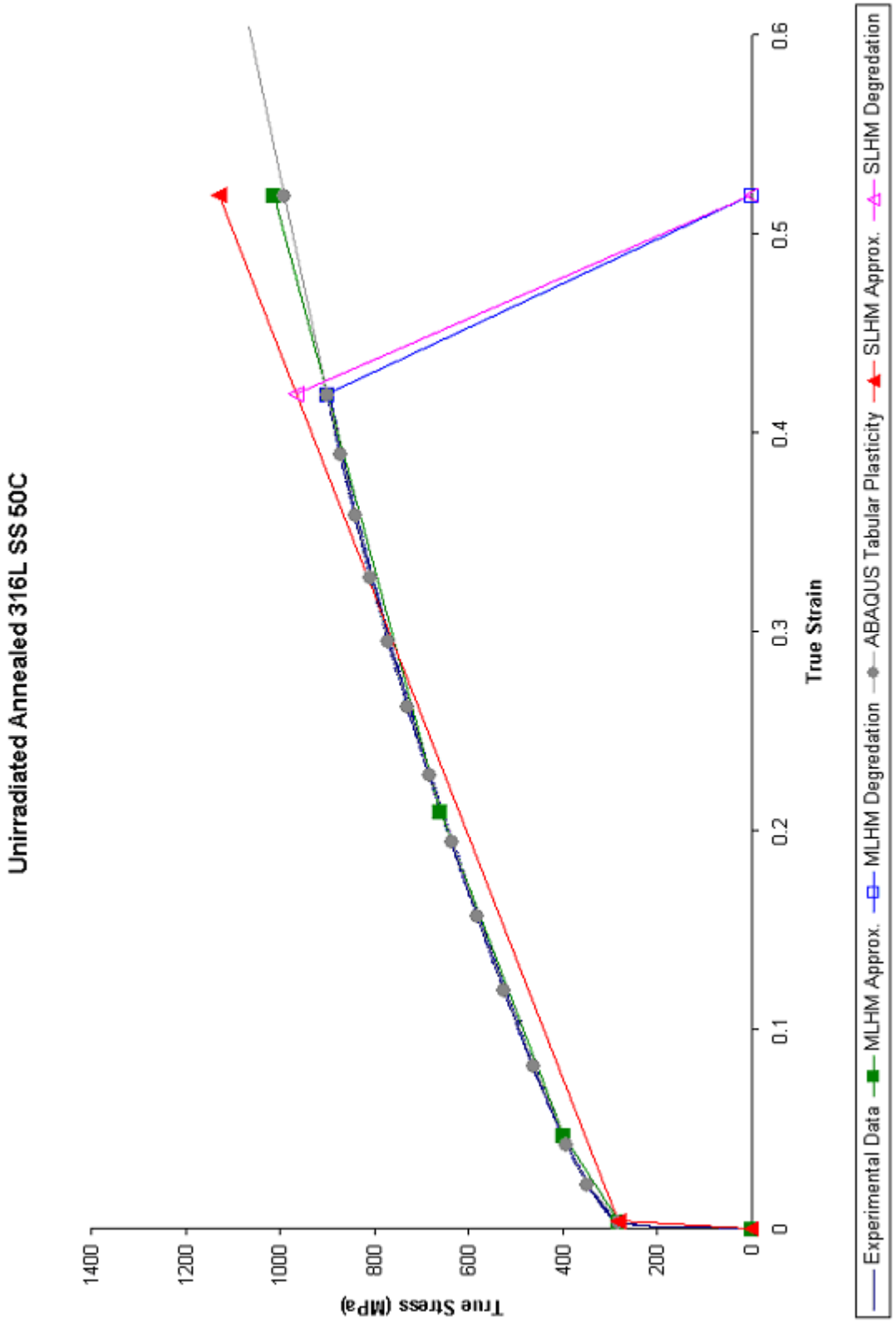

Figure 4.3. True Stress – True Strain Curve Comparison

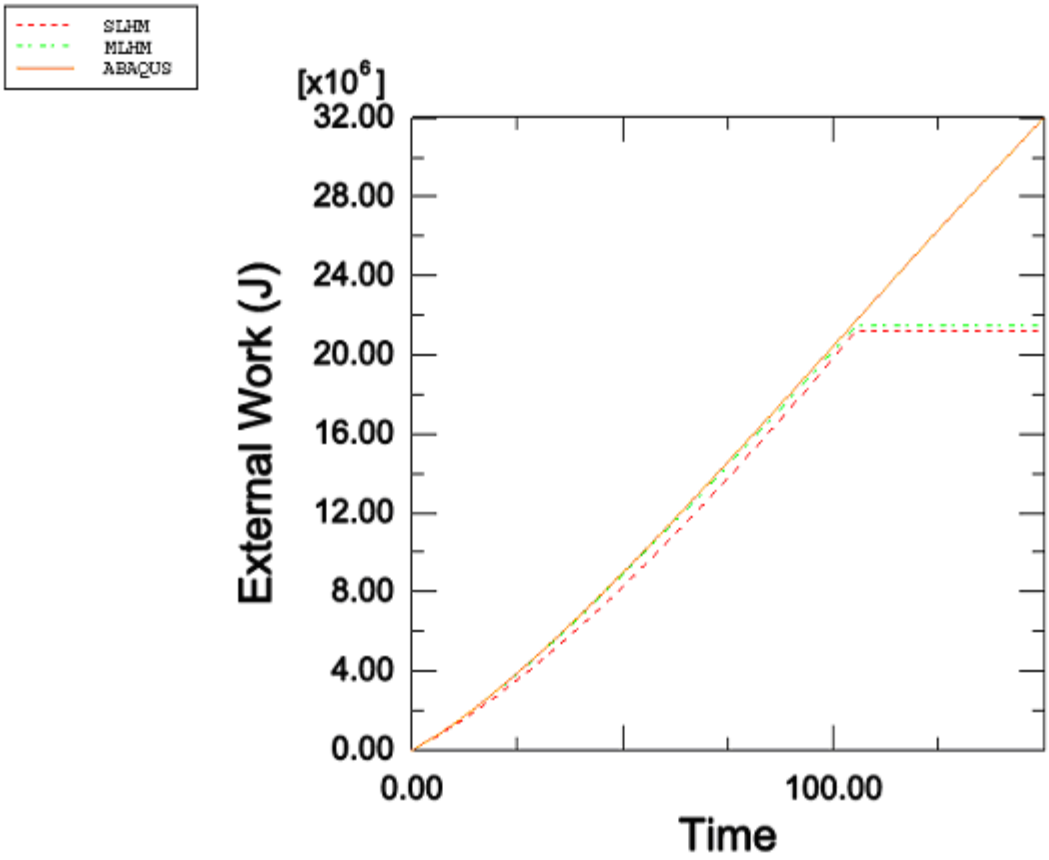

Figure 4.4. External Work of ABAQUS Plasticity, MLHM, and SLHM.

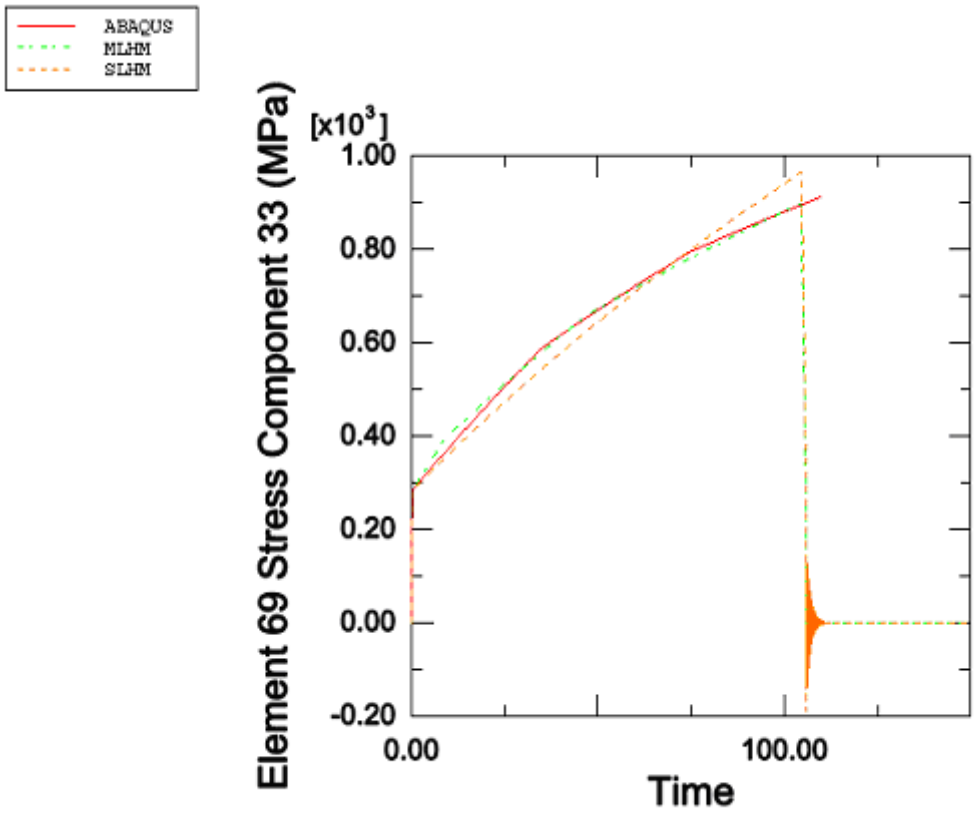

Figure 4.5. Stress Comparison.

5. FINITE ELEMENT MODELING

The finite element models were created in two ways: using ABAQUS CAE and manually modifying ABAQUS CAE created input files. All models were originally created using ABAQUS CAE to create the geometry, mesh, and boundary conditions. For some cases it was easier to manually alter and rename such input files, than to copy and alter them in ABAQUS CAE, especially when only the material properties changed from one case to the next.

There are a multitude of geometries used in these studies. The first of which is a flat tensile specimen as seen in Figure 5.1. This specimen was used to determine the appropriate fracture strain assuming damage begins at the ultimate tensile strength and continues linearly to the fracture strain as explained in section 4. An initial guess of the fracture strain is used in the material description. ABAQUS Explicit simulates the fracture of the specimen using one of the two user subroutines mentioned previously. The fracture energy determined by ABAQUS Explicit is then compared to experimental fracture energy and the user defined material properties for the subroutine are adjusted accordingly. This was repeated until the fracture energy from ABAQUS Explicit matched within 5% of the experimental value.

The second geometry is a round smooth tensile specimen without any notches or cracks. This specimen was used to verify the choice of fracture strain by comparing the fracture energy with experimental results. The third basic geometry is seen in Figure 5.2. It is the same as the second geometry except that there is a notch or crack in the middle of the gauge length that follows the circumference of the cross sectional area. The angle, depth, and shape of the notch/crack are varied. The following sub-sections will describe the elements, symmetry, mesh refinement and mass scaling used in these studies.

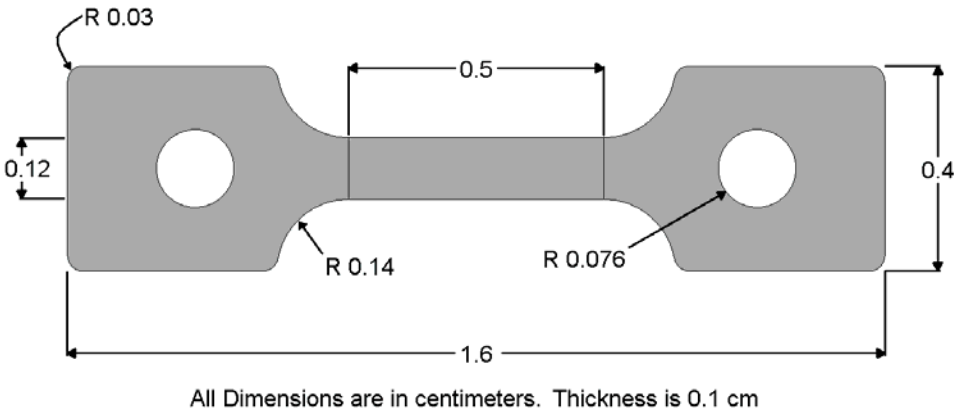

Figure 5.1. Flat Tensile Specimen

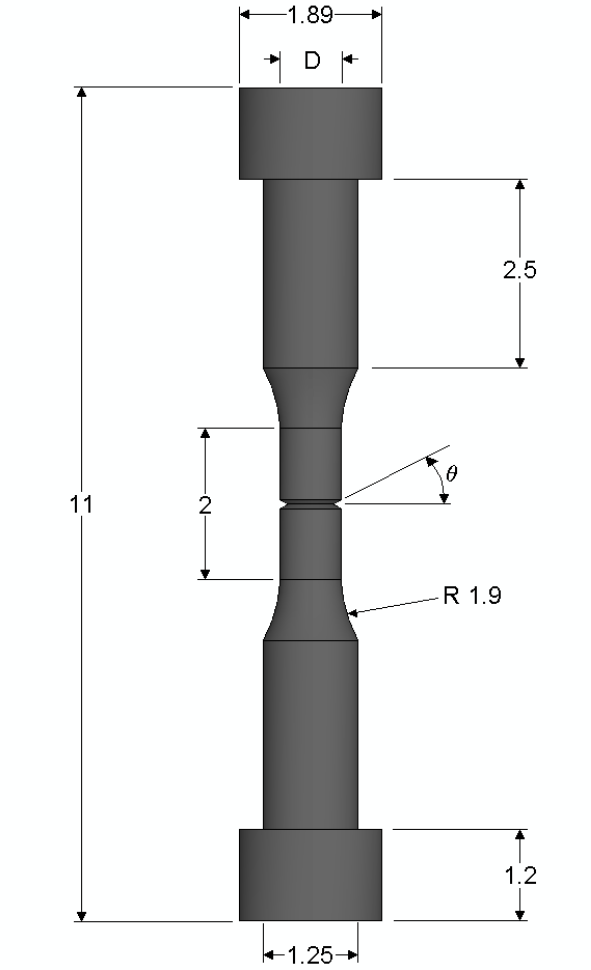

Figure 5.2. Round Tensile Specimen

5.1 ABAQUS FINITE ELEMENTS

All models that were used were created with 3D or axis symmetric elements. The 3D elements in particular are solid, continuum stress/displacement, 8-node linear brick, reduced integration, hourglass controlled elements, with the designation of C3D8R. The axis symmetric, or axisymmetric, elements are continuum stress/displacement, axisymmetric, 4-node, hourglass controlled, bilinear elements with reduced integration and a designation of CAX4R. Each 3D nodal calculation point, has three degrees of freedom, that is, it can be displaced in the x, y, or z direction. The axisymmetric calculation points have only 2 degrees of freedom. Recall the displacement and acceleration relationships from the simplified explicit algorithm presented in section 3.

Reduced integration means that the elements only have one integration point for elemental calculation instead of the usual 8 for a C3D8, or 4 for a CAX4, element. The reduced integration element allow for low run times since less values are determined for the element. The use of reduced integration elements had been verified by ABAQUS to have nearly identical results with their standard element counter-parts [16].

Hourglassing can occur with the use of reduced integration elements. Since there is only one integration point in the element, it is possible that the element can be distorted in such a way that the calculated strain becomes zero. This can lead to uncontrolled distortion in the mesh and cause inaccurate results. Hourglassing control comes standard with all first-order, reduced integration elements in ABAQUS Explicit, to alleviate this possible issue. Another way to reduce the possibility of hourglassing is to have a fine mesh where considerable distortion is likely to occur.

5.2 SYMMETRY

As mentioned in section 3, the more refined a mesh is the longer it would take for the computer to run the job in ABAQUS Explicit. One way to reduce the number of elements is by using symmetry in the model. The model is reduced to just $1/8^{th}$ of its original geometry and has symmetry boundary conditions on three of its surfaces (Figure 5.3). The surface with symmetry boundary conditions in the X direction, are not able to move in the X direction or rotate in the Y or Z directions. However the surface can expand in the Y or Z direction. This behavior is the same at the symmetry surface as if there were a mirror image of the part there instead. Likewise the symmetry conditions for Y and Z directions are not able to move in their respective direction and can not rotate in the other two directions.

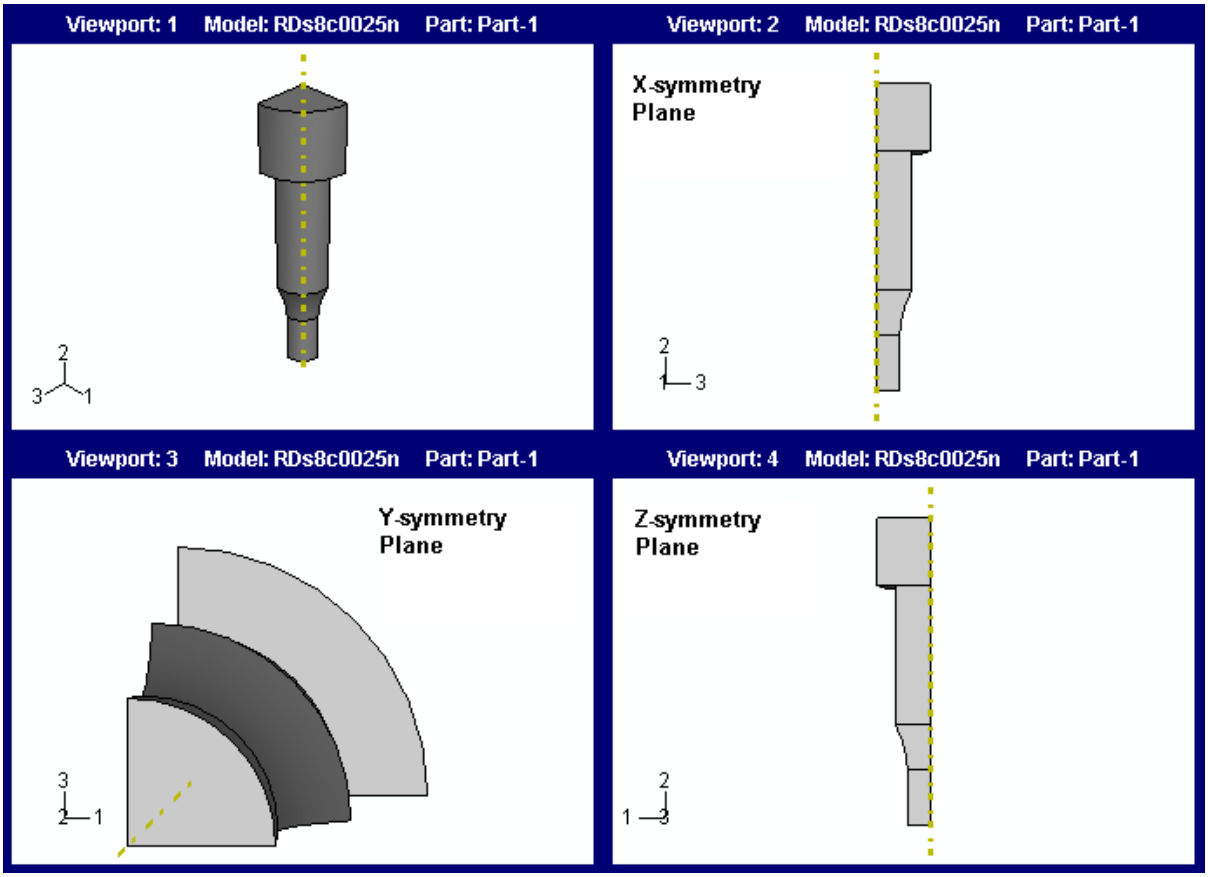

Figure 5.3. Symmetry Surfaces for a $1/8^{th}$ Specimen.

When examining the total energies, such as fracture energy, one must account for the symmetry used in the model. If $1/8^{th}$ symmetry is used, the total energy must be multiplied by 8. A possible draw back of using symmetry is that if there is a problem in that symmetric piece, like excessive distortion, than the error in the results would be multiplied accordingly. To avoid such a situation, one should visually inspect the resulting shape of the geometry after the simulation.

To ensure that the symmetry is properly used and has the same or at least very similar results to a full size model, a smooth round tensile specimen was modeled with and without symmetry. The mesh size, velocity, and direction of the tensile load were the same in both cases.

More than one symmetry test was conducted. Using the rectangular bar from section 4.3 the meshing of the bar was doubled so that the $1/8^{th}$ symmetry of the bar would have at least a cross section of 2 x 2 elements. It was determined that the fracture energy of the symmetry case was 0.28% higher than that of the full rectangular bar. Two cracks, which were $1/4^{th}$ thickness deep each, were added to the rectangular bar. They were perpendicular to the length of the bar and directly across from each other. The symmetry case was 0.95% higher than the full bar. The relative difference between the $1/8^{th}$ symmetry rectangular bar and the full bar was not constant from one case to the next due to the inclusion of the cracks.

Similarly the symmetry of a round specimen was investigated. The $1/8^{th}$ symmetric round specimen absorbed the same amount of energy prior to fracture as the full specimen. A crack was introduced on the circumference of the middle of the gauge length. The crack was $1/4^{th}$ the radius deep. The symmetric case was 0.45% higher than the full specimen.

Another form of symmetry was investigated. The round specimen is symmetric around its axis and therefore, axisymmetry can be used to represent it. Axisymmetry uses special elements described in the previous section, that allow for the round specimen to greatly reduce the number of elements and therefore run time. Using axisymmetry the difference between it and a full specimen model for a smooth gauge length was 0.13%. When a crack was introduced the difference increased to 2.81%.

The use of symmetric specimens increases the amount of energy absorbed. In all cases the symmetric specimens had a slightly higher amount of energy absorbed than the full specimen. This is due to the fact that full specimens have only one row of elements deleted while the symmetric specimens effectively have two rows of elements deleted. Since each elemental calculation is conducted individually, the elements in the full specimen would have one row ever so slightly reach the fracture strain before the neighboring elements do. This ever so slight difference does not appear in the symmetric model since the symmetry effectively calculates the strain for the elements on the symmetry plane at the same time.

The relative difference between similar geometries using symmetry is inconsistent. In the rectangular bar symmetry study, the cracked symmetric specimen absorbed more energy than the smooth $1/8^{th}$ symmetric version relative to the full specimen model. The differences between the energy absorbed by the smooth and cracked versions of both specimens were not the same. The axisymmetric model had the highest differences with the full round specimen. One possible cause in that the elements only have 2 degrees of freedom and would not include any stress relief from a third direction resulting in additional accumulated energy. Axisymmetry is solving a 3D problem in 2D which results in an increase in fracture energy

as observed by McCoy [15]. It is also plausible that the difference would decrease if the asymptotic mesh size was used. Mesh refinement is examined in the next section.

The slight changes in the geometry model affect the difference between the full and symmetric models. Therefore, a standardized correction factor for the use of symmetry is not possible for these studies. The differing forms of symmetry will only be compared to their own form to eliminate the additional differences added by using different forms of symmetry.

5.3 MESH REFINEMENT

All finite element models have some number of elements. Calculations are made for each element and corresponding nodes or integration points. Typically, the more elements a model has, the more accurate the results would be. Whenever there is a concentration of stress, deformation, energy absorbed, etc. the elements at the location need to be small enough to accurately capture the distribution of such properties. However, as seen in Equation 3.11, the more elements one has the longer the computational time.

A mesh is the separation of the geometry into elements. A large mesh size, or coarse mesh, would result in a low number of elements, whereas, a small mesh size, or fine mesh, would have a large number of elements.

A balance between coarse meshing and accuracy must be achieved. One could start with a uniform coarse mesh and incrementally reduce the mesh size until an asymptotic or near asymptotic solution is achieved. Regions that are sufficiently far from the stress concentrators, cracks, notches, sharp angles, etc., can have their mesh sizes increased provided that it does not alter the resulting fracture energy or energy dissipation. This reduces the total number of elements and saves computational time.

Whenever the geometry changes, such as deepening a crack or increasing a notch angle, the mesh also changes. It is impractical to determine the asymptotic mesh size for each and every specimen with a slight change in geometry. Therefore, an axisymetric specimen with and without a crack that is 0.1 cm deep was used to determine a target meshing scheme for all other round specimens with and without cracks or notches.

The smooth specimen was insensitive to the mesh size as can be see in Table 5.1. The mesh size was varied incrementally from the length of a square element side of 0.1 cm to 0.02 cm. There appears to be a slight increase in the fracture energy as the mesh size is reduced. The change in fracture energy was negligible, less than 0.7 J out of about 307 J, and therefore, does not warrant further consideration.

Table 5.1. Smooth Round Specimen Meshing Sensitivity Results

Uniform Mesh Size (cm)	Number of Elements	Fracture Energy (J)
0.1	366	306.5
0.08	558	306.8
0.06	937	307.0
0.04	2137	307.1
0.02	7885	307.2

From a uniform mesh size of 0.02 cm, the mesh size of regions away from the crack was coarsened to reduce the total number of elements. Table 5.2 displays the mesh size of the regions and its effect on the fracture energy. As can be seen, coarsening these regions had a negligible impact.

The search for the asymptotic mesh size for the cracked specimen starts with the last mesh sizes listed in Table 5.2. As the mesh size continues to decrease the specimen geometry was further divided to allow for different mesh sizes. The length of one side of a square element, referred to as mesh size, of the gauge length near the crack continually was reduced between the divisions and mesh coarsening. Each time the mesh size was coarsened the impact on fracture energy was negligible. Figure 5.1 shows that as the mesh near the crack is decreased in size, an asymptotic solution is approached. The actual solution was not quite reached due to the drastic increase in run time as the mesh size was reduced.

Table 5.2. Round Cracked Specimen Coarsening of Meshing Size Sensitivity Results

Mesh Size (cm)				Number of Elements	Fracture Energy (J)
Grip/End	Shank	Fillet	Gauge Length		
0.02	0.02	0.02	0.02	8005	65.5
0.12	0.02	0.02	0.02	5505	65.2
0.12	0.12	0.02	0.02	2485	65.3

Table 5.3 shows the last few mesh sizes, number of elements, the time it took to obtain the fracture energy, and the fracture energy itself. The difference in fracture energy in Table 5.3 is clearly reducing as the mesh size decreases. The run times have dramatically increased. It is impractical to use the smallest mesh size in the table or an even smaller mesh size due to the run times. A mesh size of 2.5×10^{-3} cm is selected as the best balance between accuracy and run times. Table 5.4 contains the final mesh sizes that were chosen and their corresponding regions. Figure 5.4 illustrates the chosen meshing scheme. The cracked

specimen is the limiting case so it will be further investigated while the smooth specimen will be used in the studies in subsections 5.4 and 5.5.

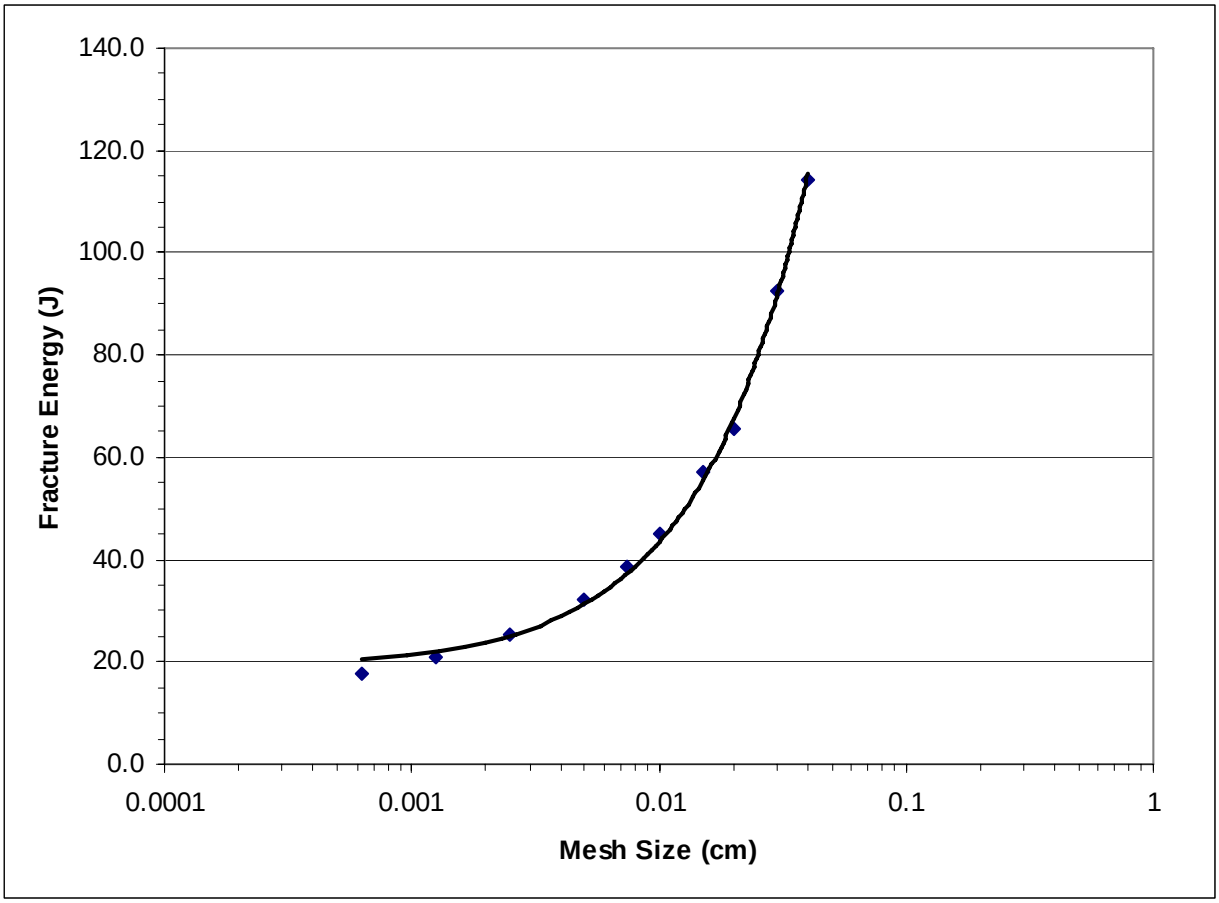

Figure 5.4. Fracture Energy vs. Mesh Size

Table 5.3. Mesh Size Sensitivity Results

Mesh Size Near Crack (cm)	**Number of Elements**	**Run Time (hrs)**	**Fracture Energy (J)**
2.5×10^{-3}	34725	4.43	25.4
1.25×10^{-4}	130725	14.77	20.9
6.25×10^{-5}	514725	~36.50	17.9

Table 5.4. Final Mesh Sizes

Region	**Mesh Size (cm)**	**Number of Elements**
Grip	0.12	80
Shank	0.12	105
Fillet Top	0.04	140
Fillet Bottom	0.02	400
Gauge Top	0.01	2000
Gauge Bottom	2.5×10^{-5}	32000

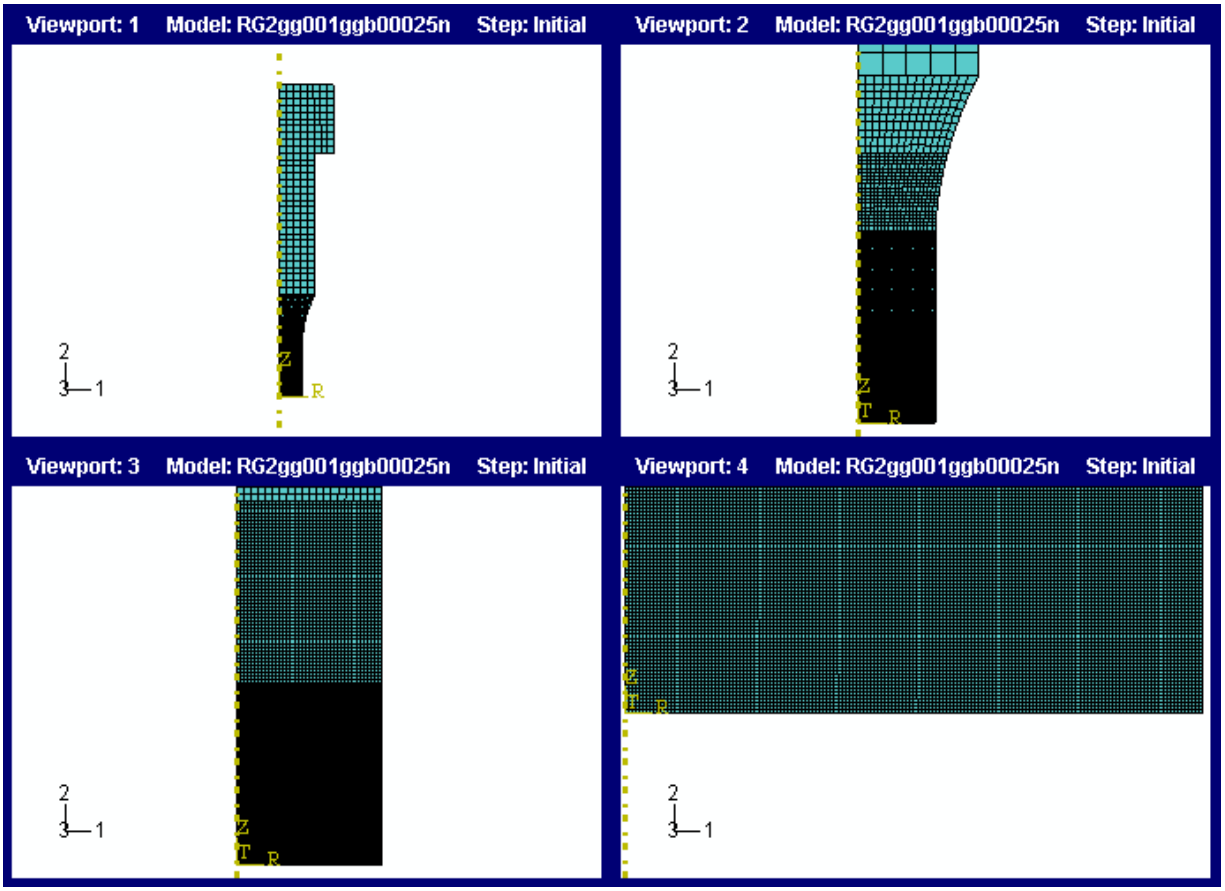

Figure 5.5. Finalized Mesh Scheme

5.4 MASS SCALING

Mass Scaling, as mentioned in Section 3, can be used to decrease the computational time of a given analysis in ABAQUS Explicit. By increasing the mass of some or all of the elements, the stable time increment would increase (Equation 3.10), and fewer increments would be necessary. Decreasing the number of increments results in decreasing the number of calculations and, therefore, reducing the total computational time (Equation 3.11).

There are multiple ways of implementing mass scaling. It can be applied uniformly to all elements or applied on an element-by-element basis. It can automatically be applied to

given elements or applied to user-specified elements. The mass scaling factor, the factor by which the mass is increased, can be specified by the user or determined automatically. It can be applied once for the whole analysis, step-by-step, or any interval of increments.

Caution must be exercised when using mass scaling since an increase in mass would increase the inertial forces and could significantly affect the results. To limit the affect mass scaling has on the results, the application is limited in all studies presented here. A target stable time increment is set by the user and at a set number of increments the mass scaling is re-evaluated for each element. Any element with a stable time increment size less than the user-specified value is multiplied by an automatically determined mass scaling factor to increase the stable time increment to the user-specified value.

Ideally every geometry and mesh combination used in the studies presented would have an analytical analysis preformed to find the asymptotic solution for the use of mass scaling. However, like the mesh refinement in the previous subsection, it is impractical to do so. The analytical solution for the mass scaling, where the target stable time increment was varied, was determined for the same specimen in the previous subsection and its chosen meshing scheme.

For all analyses a visual inspection of the resulting deformation was used to reveal erroneous behavior in the analysis. An example of such behavior would be the deletion of elements that are not on the symmetry plane. Such deletion could appear as a propagation of multiple cracks in the flat or round specimens. Often times if extra elements are deleted it is the result of too high of a selected target stable time increment size. One simulation had broken 137 extra elements out of the 32,000 in the gauge bottom and resulted in 0.7% higher

fracture energy. This shows that deletion of extra elements can slightly increase the resulting fracture energy and excessive deletion of extra elements should be avoided.

Table 5.5 contains the results of varying the target time increment size. The largest increment size resulted in almost twice the fracture energy due to the creation and propagation of multiple cracks. The second largest increment size results in 1.5 J increase over the lowest fracture energy in the table. Clearly the asymptotic solution is being approached. The second to last target time increment is only 0.5 J higher than the lowest fracture energy. It also runs about 5 times faster than the smallest increment size. The target time increment size of 5.0 x 10^-6 is chosen for its balance of accuracy and computational time.

Table 5.5. Variation of Mass Scaling Target Time Increment Size

Target Time Increment (s)	Fracture Energy (J)	CPU Time (min)
5.00E-05	46.6	4.00
1.00E-05	26.9	15.00
5.00E-06	25.9	30.45
1.00E-06	25.4	156.57

Table 5.6 shows that the fracture energy and computational time are independent of the frequency of the mass scaling determination. A frequency of 10 means that after every 10 increments the amount of mass scaling and the elements it is applied to is recalculated. The fracture energy is the same regardless of the mass scaling frequency. The computational time is relatively constant. The minor fluctuations in the amount of time for the simulations could

be the result of fluctuations of other programs that are running in the background. A frequency of 10 is chosen since it was used in the previous subsections.

Table 5.6. Variation of Mass Scaling Frequency

Frequency	Fracture Energy (J)	CPU Time (min)
1	25.9	30.51
10	25.9	30.45
100	25.9	29.73
1000	25.9	29.91
10000	25.9	31.81

5.5 CROSS HEAD SPEED

The speed at which the specimen is pulled is referred to as the cross head speed. The experimental data for 316 SS used a cross head speed of 0.0005 cm/s. The resulting stress strain curves from those experiments were approximated using the multi-linear hardening modulus model explained in subsection 4.2. The analysis is independent of the cross head speed because only one stress strain curve is provided thus making it rate-independent. As proof, the same specimen, meshing, and mass scaling used and determined in the previous subsection has its cross head speed varied with the results shown in Table 5.6.

Table 5.7. Variation of Cross Head Speed

Cross Head Speed (cm/s)	Fracture Energy (J)	CPU Time (min)	CPU Fracture Time (min)
0.125	25.5	59.33	34.36
0.25	25.9	56.60	16.41
0.375	26.4	57.76	11.41
0.5	26.9	57.76	8.76

The cross head speed was varied by 0.125 cm/s over the range of 0.125 to 0.5 cm/s. The fracture energy varies by almost 1.5 J. The 0.375 and 0.5 cm/s cases had 17 and 13 additional elements break. These failed elements are not on the symmetry crack plane. They failed due to increased stress and strain that resulted from the instability introduced by the overly increased cross head speed. The increase in the stress and strain also results in additional absorption of energy, thus increasing the fracture energy. There is a slight difference between the 0.125 and 0.25 cm/s cases due to the same phenomenon except no additional elements were fractured between the two.

CPU fracture time was also presented with CPU time because the CPU time is virtually independent of the cross head speed. CPU time depends on symmetry, mesh size, mass scaling, and the simulated time. Simulated time is the time that ABAQUS represents within the simulation. It is specified by the user and can be adjusted to match the simulated fracture time so that extra time after fracture is not simulated, thus reducing the overall CPU

time. Adjustment of the simulated time requires fore knowledge of when the specimen would fracture. As a result, throughout the remaining studies where fracture time is unknown, a conservative value should be used. If the simulated time is shorter than the fracture time, then the specimen would not at least completely fracture. The simulation would have the simulated time increased and the simulation repeated to include the fracture of the specimen.

The 0.25 cm/s case appears to have the best balance of CPU fracture time verses accuracy. It will be used for the remaining simulations.

5.6 FINAL MODELING PARAMETERS

In the previous subsections (5.1 through 5.5), decisions were made concerning what types of elements and symmetry to use, as well as, meshing scheme, mass scaling target time increment size, and cross head speed. Table 5.8 displays the final parameters chosen for the remainder of the simulations.

Table 5.8. Final Modeling Parameters

Parameter	**Value**
Elements	CAX4R
Symmetry	Axis Symmetry (axisymmetry)
Mesh Size for Grip (cm)	0.12
Mesh Size for Shank (cm)	0.12
Mesh Size for top of Fillet (cm)	0.04
Mesh Size for bottom of Fillet (cm)	0.02
Mesh Size for top of gauge length (cm)	0.01
Mesh Size for bottom of gauge length (cm)	6.25×10^{-5}
Target Time Increment Size (s)	5.00×10^{-6}
Mass Scaling Frequency (increments/scaling)	10
Cross Head Speed (cm/s)	0.25

6. MATERIAL PROPERTIES

Experimental data was used as a basis for the true stress and true strain input for ABAQUS Explicit. The unirradiated data was provided by Professor James Stubbins of the Nuclear Engineering Program at the University of Illinois Urbana – Champaign in the form of engineering and true stress-strain data points. Irradiated data came from [3]. The first two subsections describe the determination of fracture energy and the multi-linear hardening modulus (MLHM) model parameters for use in the subsections thereafter.

6.1 DETERMINATION OF FRACTURE ENERGY

Fracture energy is the area under the load – displacement curve [1]. The engineering stress – strain data can be converted to load – displacement data given dimensional information of the specimen.

Engineering stress can be converted to load using Equation 6.1. Engineering stress (S) was provided in megapascals (MPa) which is equal to Newtons per millimeter squared (N/mm^2). Load (P) would be the force in Newtons (N) that is applied. The cross sectional area of the specimen (A) is multiplied to the engineering stress to get the load. The cross sectional area is in unit of cm^2, so a conversion factor (C) is included, where C = 100 mm^2/cm^2.

Equation 6.1. Determination of Load from Engineering Stress

$P = S \times A \times C$ In terms of units: $N = (N/mm^2) \times (cm^2) \times (100\ mm^2/cm^2)$

Engineering Strain is converted to displacement using Equation 6.2. Engineering strain (e) is any unit of length above itself, for example cm2/cm2. The original length (L) of the specimen is then multiplied by the strain to get the displacement (d). Since the flat and

round specimens do not have uniform cross sectional area the gauge length is used as the original length. The gauge length of these specimens is defined for these studies as the length of the round central portion of a specimen between the two fillets. The cross sectional area used in Equation 6.1 is that of the gauge length. This assumes that the deformation and displacement only take place in the gauge length. The assumption is acceptable only if negligible amounts of deformation take place in the remainder of the specimen. Most likely some energy will be absorbed in the fillets of a smooth specimen. The following subsection will address this issue.

Equation 6.2. Determination of Displacement from Engineering Strain

$d = e \times L$ In terms of units: cm = cm/cm x cm

A program called Origin 7.5 [17] was used to determine the area under the load – displacement curve for each specimen type and material used in these studies. Equations 6.1 and 2 were used in spreadsheets to convert the stress and strain to load and displacement. Load and displacement was imported into Origin 7.5 and a graph was created from it. A feature called “Integrate” was used to calculate the area under the curve which is the fracture energy [1].

Table 6.1 shows the fracture energy as determined by the method described above. The unirradiated 316L SS at 50°C is presented for both the flat and round specimens.

Table 6.1. Fracture Energy of Specimen Materials

Material	Fracture Energy of Specimen (J)	
	Flat	**Round**
Unirradiated	1.845	310.8
Irradiated to 0.78 dpa	N/A	275.5

6.2 DETERMINATION OF MLHM PARAMETERS

As mentioned in Section 4.2, there are many user defined parameters for the material properties used with the MLHM failure method Poison's ratio is known for the unirradiated annealed 316 SS at 50°C to be 0.3 and is assumed to be the same for the irradiated case. To test this assumption poison's ratio was changed to 0.15. The difference in fracture energy between the 0.3 and 0.15 cases was about 0.1% and is negligible for these studies.

The yield stress depends on the material and is taken as the stress at the intersection of the 0.02% offset of the elastic modulus with the experimental data provided by Prof Stubbins of the University of Illinois at Urbana. The hardening modulus parameters were chosen by the user to approximate the experimental data in the plastic deformation region, see Figure (in section 4.2). The damage initiation plastic strain and the failure strain are unknown in the true stress and true strain curve since the correlation with the engineering stress – strain is no longer valid beyond the UTS.

The damage initiation plastic strain and failure strain are determined through a series of simulations which adjust these parameters to match the fracture energy of the test

specimen as shown in Table 5.1. The damage initiation plastic strain is assumed to be the UTS since that is where the specimen starts to neck and localized deformation can be visually seen. The first attempt to match the fracture energy of the simulation with the experimental value uses a 0.1 offset. This means that the strain between the damage initiation and failure is 0.1. The damage initiation plastic strain or failure strain is then adjusted for the following attempt and continues to be adjusted until the fracture energy is within 5% of experimental values as determined in section 6.1.

The flat specimen was chosen for this iterative process for the unirradiated material since it was originally used to generate the experimental data [18]. Also the flat specimen model has fewer elements than the round specimen model and therefore, the flat specimen simulations have shorter run times. Once MLHM model parameters are determined they are used with the smooth round specimen geometry to verify that the chosen strains result in the appropriate fracture energy.

The process was conducted for unirradiated 316L SS at 50°C and an irradiated specimen which accumulated 0.78 displacements per atom. Such an irradiation level means that on average each and every atom in the specimen was displaced from its lattice position 0.78 times. The table below shows the material properties used for both cases.

Table 6.2. Material Properties for Unirradiated and Irradiated 316L SS at 50°C

Parameter	Unirradiated	Irradiated at 0.78 dpa
Young's Modulus (10^{-1} Pa)	1.93×10^{12}	2.744×10^{14}
Poison's Ratio	0.3	0.3
Damage Initiation Plastic Strain	0.415628	0.3225
Failure Strain	0.515628	0.4225
Yield Stress (10^{-1} Pa)	2.84×10^{9}	6.9×10^{9}
Hardening Modulus #1 (10^{-1} Pa)	2.65413×10^{10}	-5.7×10^{9}
Plastic Strain #1 (Initiates use of Second Hardening Modulus)	0.0413818	0.017
Hardening Modulus #2 (10^{-1} Pa)	1.59454×10^{10}	1.575×10^{10}
Plastic Strain #2 (Initiates use of Third Hardening Modulus)	0.206128	0.21
Hardening Modulus #3 (10^{-1} Pa)	1.15361×10^{10}	1.21×10^{10}

6.3 VARIATION OF RADIUS AND ITS EFFECT ON FRACTURE ENERGY

Two methods were used to determine the fracture energy at varying radii of the gauge length of a smooth round specimen of unirradiated 316L SS. The first of which is the method

described in Section 6.1, using the experimental stress-strain curves and the specimen dimensions. The second method uses ABAQUS and the material properties listed in Section 6.2. Figure 6.1 shows the comparison of the two methods.

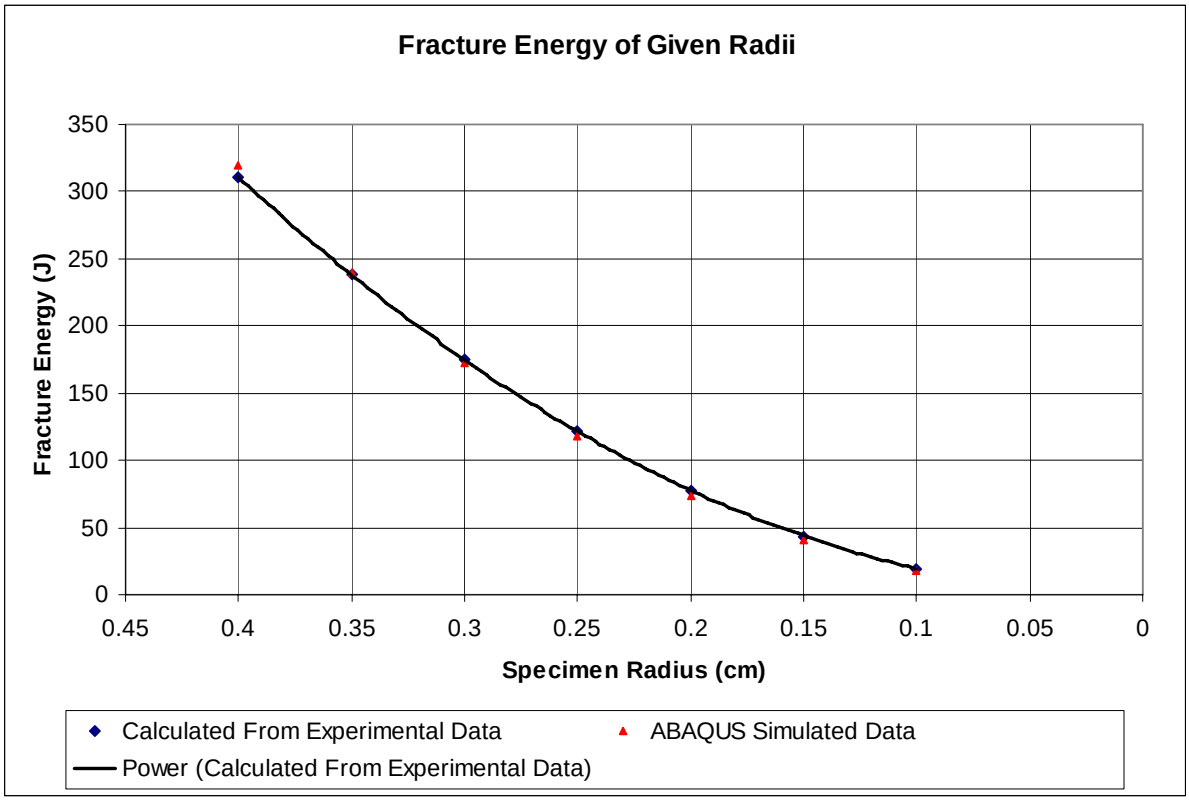

Figure 6.1. Fracture Energy vs. Gauge Length Radius

The two methods are in good agreement with each other. On average ABAQUS matched the experimentally determined fracture energy within 4%. The closet comparison was at a radius of 0.35 cm with ABAQUS over predicting by 0.8%. The worst comparison was at a radius of 0.1 cm which under predicted the fracture energy by 12%. Considering that the experimental fracture energy for a radius of 0.1 cm was only 19.43 J and ABAQUS determined it to be 17.15 J, the absolute difference is only 2.28 J.

In general, a radius of 0.4 cm seems to over predict, while radii 0.3 cm and less consistently under predict the fracture energy. Radius 0.35 cm matched rather well. This occurs as a result of energy deposition in to the fillet of the specimen. The experimentally calculated fracture energy assumes that only the gauge length is absorbing the plastic energy. Recall that the material properties were determined with the flat specimen. These properties were chosen to match the total fracture energy of the flat specimen (energy in fillets included) to the experimentally calculated fracture energy. The fillet of the 0.4 cm radius specimen has a smooth transition that allows more energy to be absorbed in the fillet of this round specimen than the flat specimen. As the radius decreases the transition from the gauge length to the fillet becomes steeper thus reducing the amount of energy absorbed in the fillet to the point of ABAQUS appearing to under predict the fracture energy.

The fracture energy as a function of the reduction of the gauge length radius follows Equation 6.3. The fracture energy (G_F) is proportional to the square of the specimen radius (r). The equation is based on the experimentally calculated fracture energy and would have a slightly different constant if the equation was based on the ABAQUS energies.

Equation 6.3. Trend of Fracture Energy as a Function of Radius

$$G_F = 1942.5\, r^2$$

7. RESULTS AND DISCUSSION

This section describes the multiple analyses that were conducted using ABAQUS Explicit and the information contained in all the previous sections. As different aspects of the geometry are varied, the impact on the fracture energy is observed. Each set of variations was conducted for unirradiated 316 stainless steel at 50°C and 0.78 dpa irradiated stainless steel specimens. A pearl script was written to automatically execute a list of simulations one right after the other. The script can be found in Appendix B.

7.1 VARIATION OF FRACTURE ENERGY WITH ANGLE FOR SHARP V-NOTCHES

A smooth (as-in no visible cracks or notches) round specimen made of annealed 316L SS at 50°C has fracture energy of about 310 J as determined in Section 5.1. A thin crack with a depth of 0.1 cm was introduced into the middle of the specimen. The crack was changed to a narrow V shaped notch with an angle of 20°. The angle increased and the depth was held constant. The same process was executed for stainless steel 316 irradiated to 0.78 dpa. The smooth specimen fracture energy of the irradiated specimen was 275 J.

Figure 7.1 shows the dependency the fracture energy has on the notch angle. The blue diamond curve (♦) corresponds to the unirradiated specimen. The fracture energy, at a angle of 0°, drops by almost a factor of 12 down to about 25 J. As the notch angle increases the fracture energy remains relatively constant until it reaches about 140° where the fracture energy is just above 25 J. The fracture energy starts to increase, and after an increase of about 20° the fracture energy is 35 J. The fracture energy increases exponentially above a notch angle of 160°. When the angle is 180°, which corresponds to a smooth round

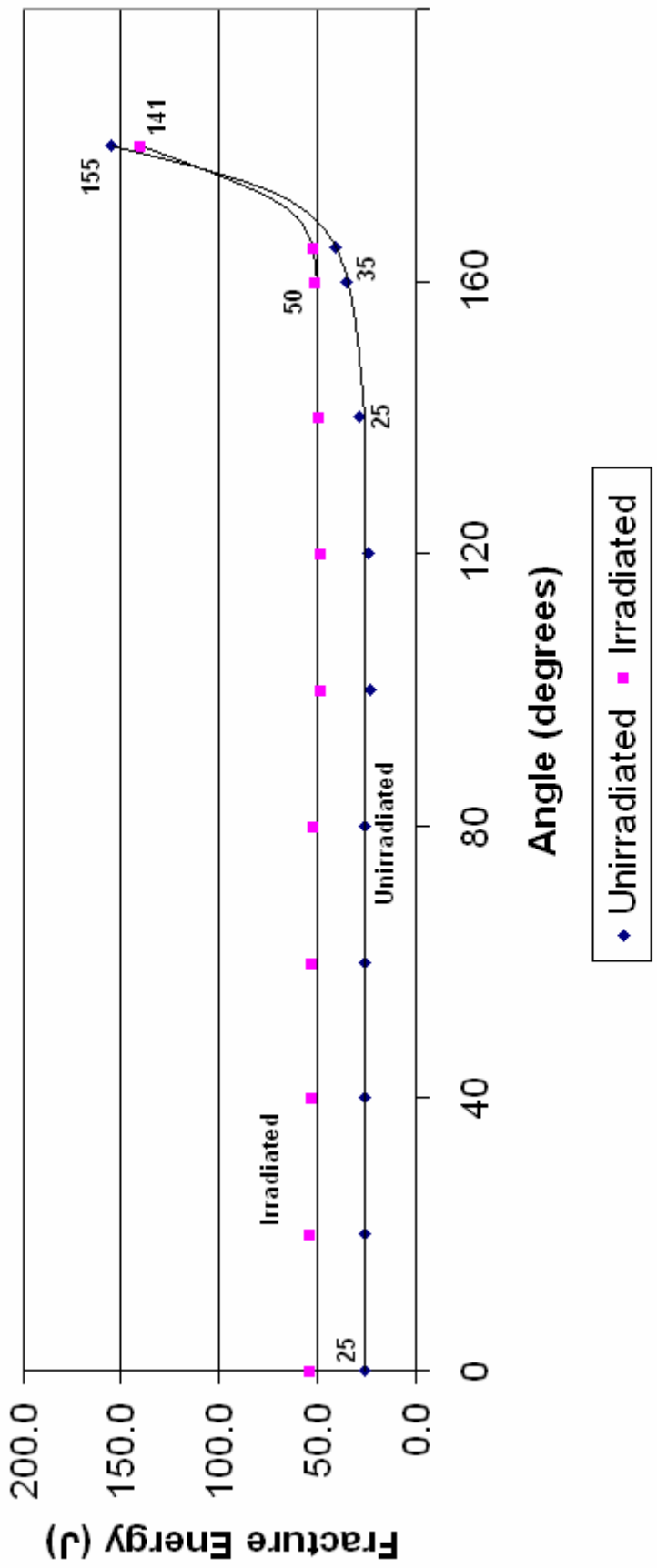

Figure 7.1. Fracture Energy vs. Notch Angle

specimen with a diameter of 0.6 cm (0.8 - 2* 0.1 cm), the fracture energy is approximately 155 J.

The irradiated specimen appears to follow a similar trend. However, the irradiated specimen remains relatively constant at first with 50 J which is twice that of the unirradiated specimen. The initiation of the exponential increase in fracture energy appears to be delayed in the irradiated specimen to just beyond 160°. Irradiated materials become more brittle than unirradiated materials with the exception of dislocation channel deformation. Since deformation primarily occurs in the dislocation channels, the irradiated specimen has less dependence on the crack angle than the unirradiated specimen. The fracture energy of the irradiated smooth specimen with a reduced diameter of 0.6 cm is 140 J which is less than it is for the unirradiated specimen (155 J) as one would expect.

The relative independence of angle on fracture energy is most likely caused by the blunting of the notch tip as the specimen elongates under tension. The tip is blunted due to a concentration of stress at that location. The stress concentration is related to the initial notch angle. As the tip blunts the stress concentration decreases and the initial notch angle becomes irrelevant.

At a given angle of 140° for the unirradiated specimen, and about 160° for the irradiated specimen the initial stress concentration is reduced to the point that the energy is distributed through more of the material and not concentrated as much at the notch tip. As the angle approaches 160° the stress concentration factor is approaching 0.

The fracture energy is almost uniformly distributed in the gauge length of the smooth round specimen before the fracture occurs. For an unirradiated notched specimen,

(Figure 7.2) the fracture energy is distributed highly non-uniformly in an ellipsoidal volume in the vicinity of the notch tip. Only a quarter of the ellipsoid can be seen in Figure 7.2 due to the use of symmetry in the model. Notice that the plastic dissipation energy density (PENER) with units of J/cm^3 is shown in Figure 7.2. The elastic energy contribution to the fracture energy is negligible (about 0.5 J for the unirradiated specimen with an angle of 180°). Although there is a substantially high energy density associated with the notch tip, the maximum energy density is the same as a specimen without a notch. With more material and better distributed energy, the smooth specimen has higher fracture energy than a notched specimen prior to fracture. In the stages just before the fracture, the fracture energy remains concentrated close to the notch tip in the ellipsoidal volume. This localization around the notch tip is primarily responsible for a reduction in fracture energy. The crack depth of 0.1 cm resulted in a reduction in fracture energy by a factor of about 12 for the unirradiated specimen.

Figure 7.3 shows that for a 140° angle notch in an unirradiated specimen the fracture remains concentrated in an ellipsoidal volume around the notch tip similar to the 60° angle notch. As the crack opening angle increases to 180° for the unirradiated specimen (Figure 7.4) the fracture energy is much more uniformly distributed in a larger volume than for 60° and 140°.

Figures 7.2, 7.3, and 7.4 have four “viewports” which display the specimen during different moments in time as it is being stretched. In Figures 7.2 and 7.3 the crack is initiated in viewport 1. Viewport 2 shows the crack a quarter of the way through the thickness. Viewport 3 illustrates the plastic dissipation energy density when the

circumferential crack is half way through the radius. Viewport 4 displays the broken specimen.

Figure 7.4 shows the 180° angle specimen with a coarse mesh. It was determined in Section 5.3 that the fracture energy is relatively insensitive to the mesh size for a smooth specimen since the energy is nearly uniformly distributed in the gauge length with some energy absorption in the fillet. Due to the considerable distribution of the energy and corresponding strain, all the elements at that would fracture reach the fracture strain at relatively the same time. Thus the crack propagation was almost instantaneous and not observed in the simulation snapshots. For this reason, a crack would propagate quicker through the smooth specimen than a notched or cracked one after crack initiation. The initiation of the crack takes much longer for a smooth specimen. The first three viewports for Figure 7.4 show the increasing plastic dissipation energy density. Viewport 4 shows the specimen after fracture occurs.

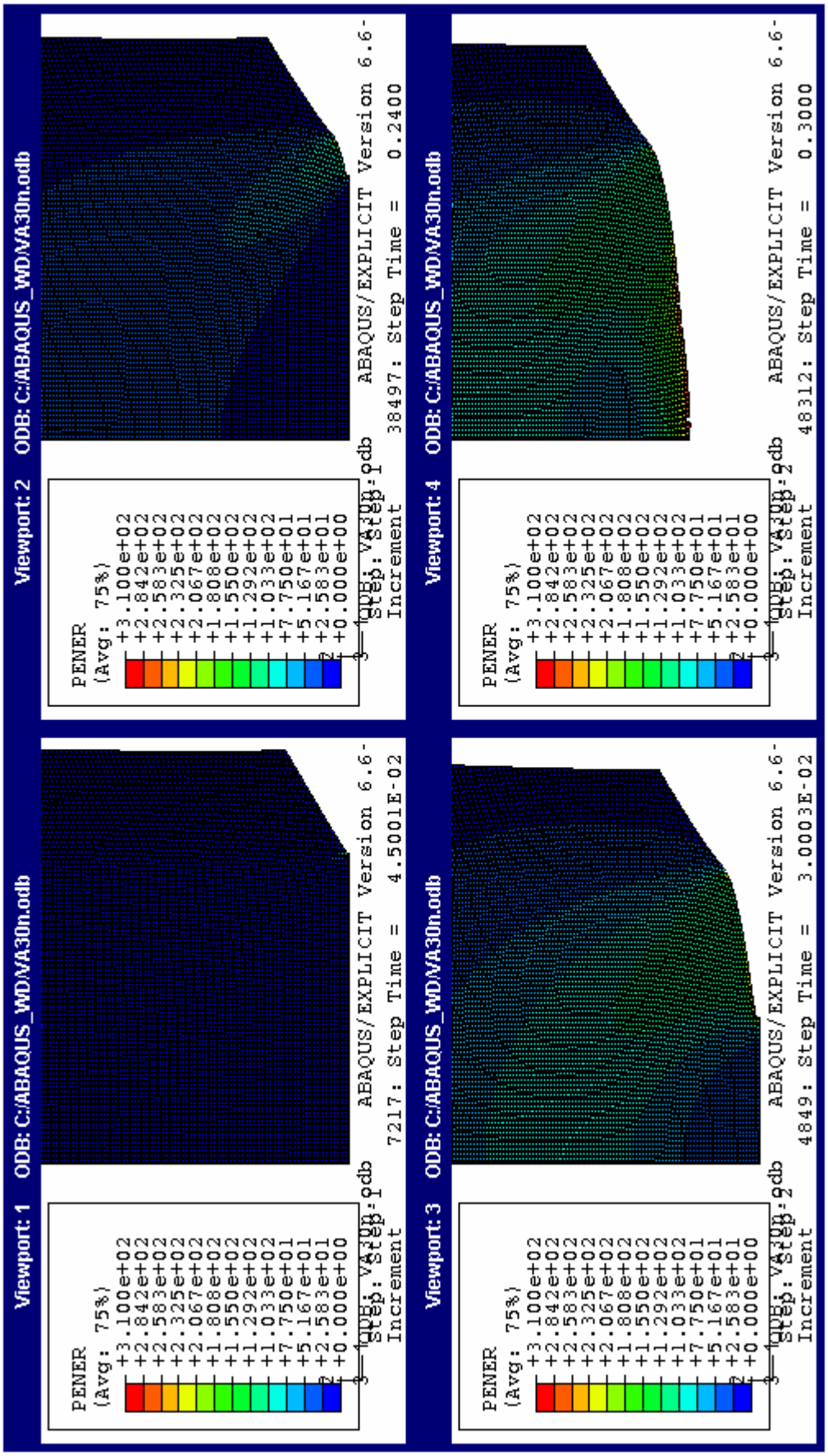

Figure 7.2. Plastic Energy Density (PENER) in J/cm³ of V-notch With 60° Angle For the Unirradiated Specimen

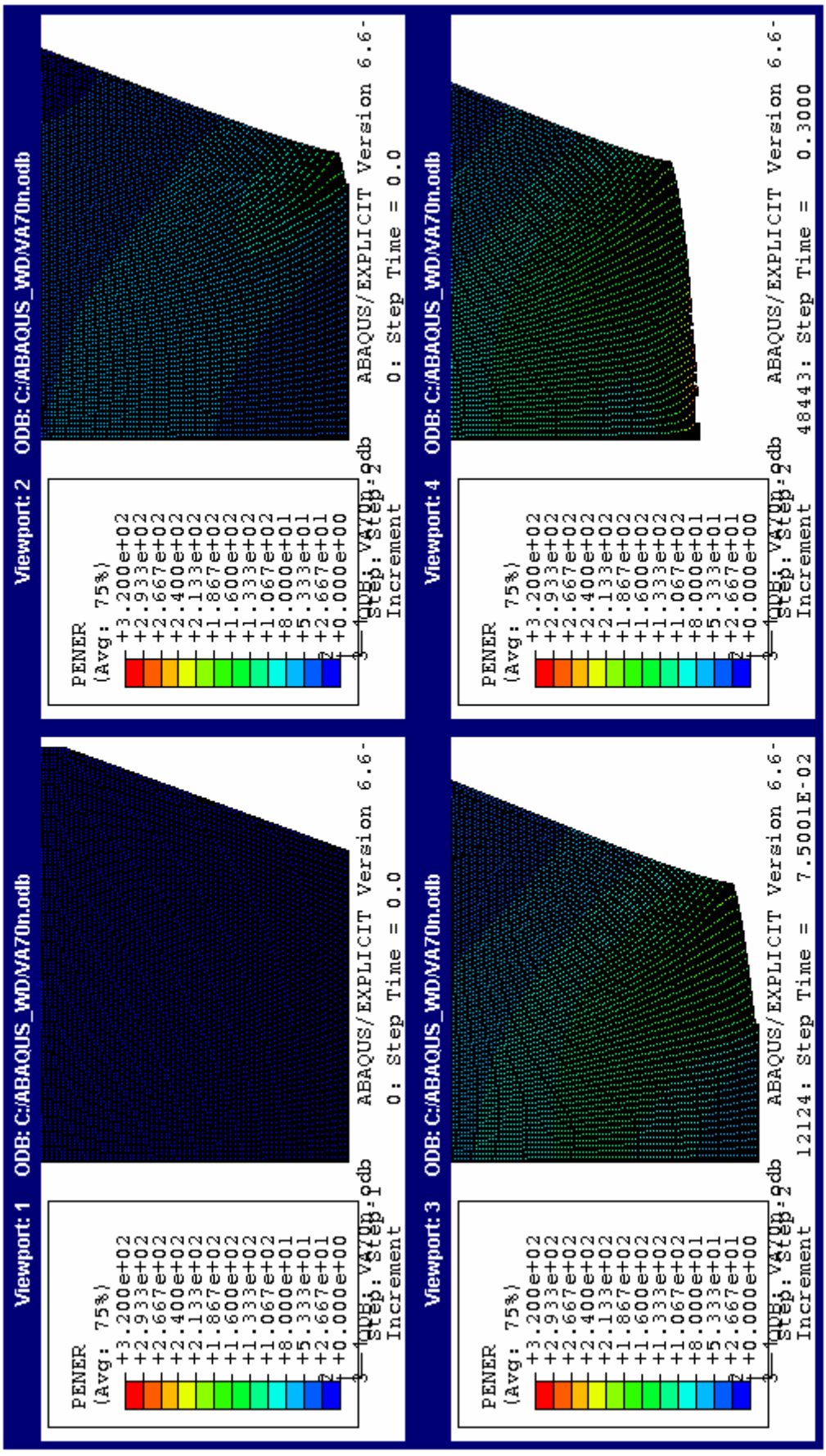

Figure 7.3. Plastic Energy Density (PENER) in J/cm^3 of V-notch With 140° Angle For the Unirradiated Specimen

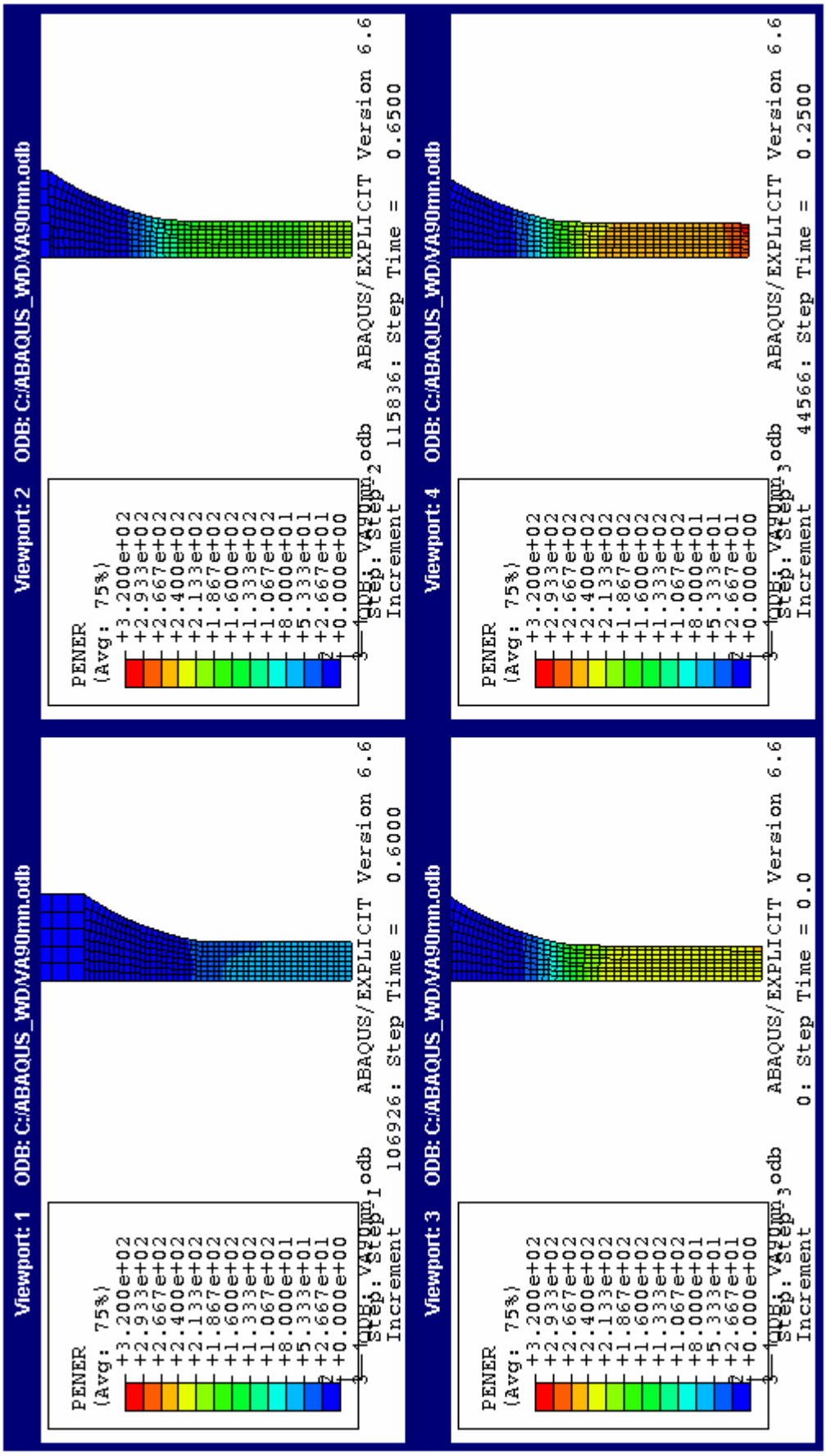

Figure 7.4. Plastic Energy Density (PENER) in J/cm^3 of V-notch With 180° Angle, or A Specimen with a Reduced Diameter Proportional to the Crack Depth, For the Unirradiated Specimen

7.2 VARIATION OF FRACTURE ENERGY WITH CRACK DEPTH

A circumferential crack was introduced at the mid-gauge length of a smooth round specimen. The crack effectively reduces the cross sectional area of the gauge length. This particular type of crack follows a trend like that of Equation 7.1 which was empirically determined with the use of the unirradiated material as described in Section 6.2 and the round specimen geometry described in Section 5. The same set of simulations was executed for a specimen irradiated to 0.78 dpa. Figure 7.5 shows both cases.

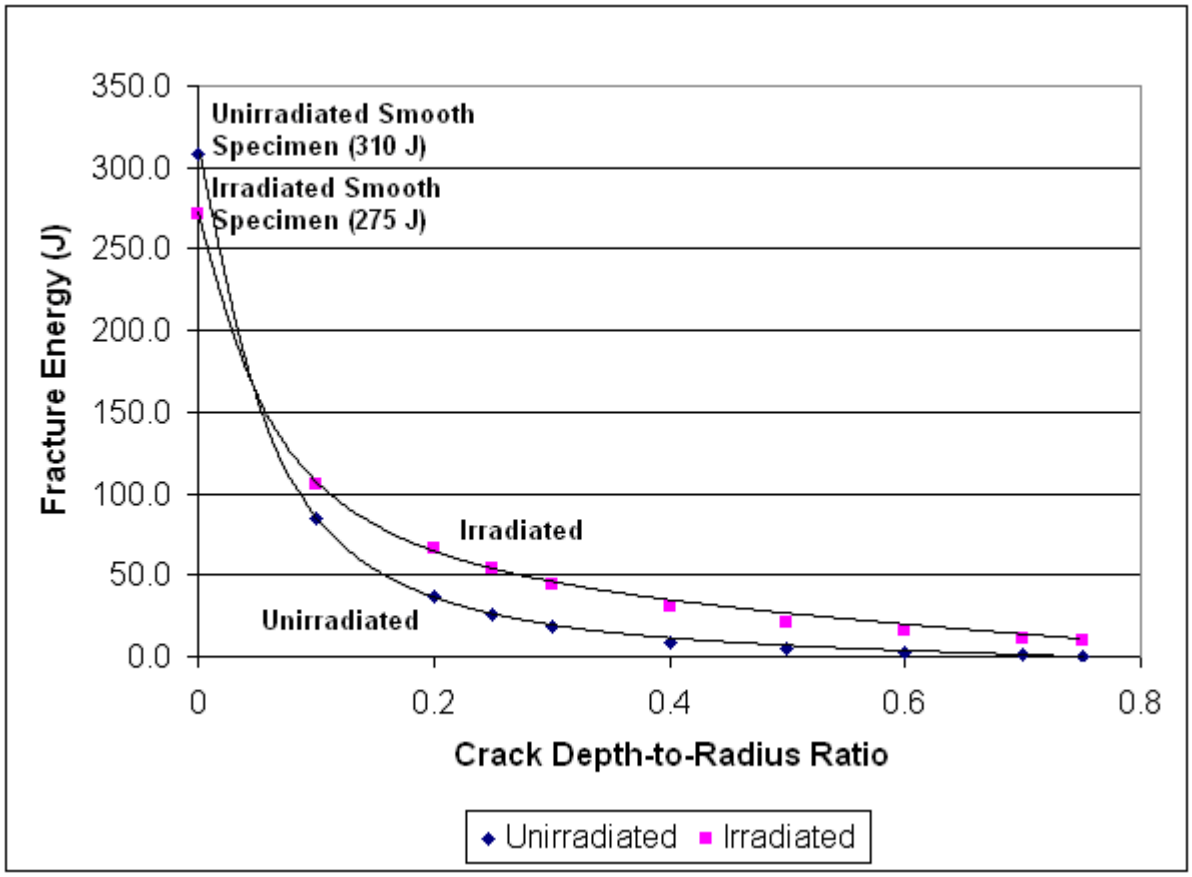

Figure 7.5. Fracture Energy vs. Crack Depth-to-Radius Ratio for Unirradiated and Irradiated SS

As seen in section 7.1, for a smooth specimen the unirradiated specimen has higher fracture energy, but when a crack or notch is present, the irradiated specimen has the higher fracture energy.

The fracture energy of a smooth specimen (G_F^0) can be used to determine the fracture energy of circumferentially cracked specimens. The crack depth (a) and the round specimen radius within the gauge length (r) are also needed. The unirradiated curve in Figure 7.5 shows the trend of Equation 7.1 and the data points used to determine the trend. It should be noted that this correlation was devised for annealed 316 SS at 50°C and would be different for other materials since the irradiated specimen fracture energy trend is different.

Equation 7.1. Fracture Energy Trend of Circumferential Crack for Unirradiated Stainless Steel

$$G_F = G_F^0 \left[1.1e^{-(a/r)/0.2} - e^{-(2.65+a/r)}\right]$$

Where

G_F^0 = fracture energy of a smooth specimen

a = crack depth

r = radius within the gauge length

The original specimen gauge length diameter was increased and decreased by 0.2 cm to create two new specimens. All diameters of the specimen were adjusted by 0.2 cm, while the heights of the specimen features (fillet, shank, etc.) remained constant.

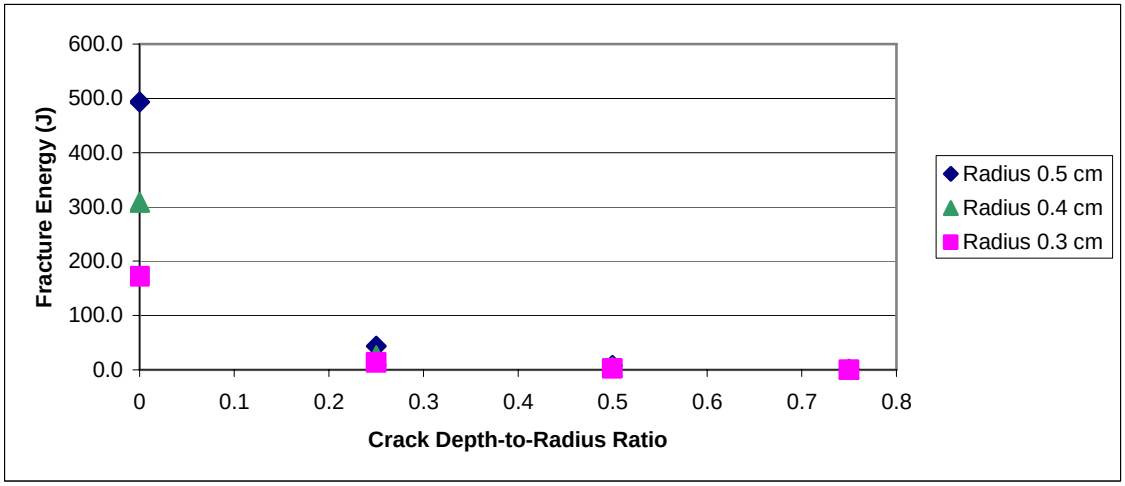

Figure 7.6. Fracture Energy vs. Crack Depth-to-Radius Ratio for Varying Radii of Unirradiated SS

Figure 7.6 and section 6.3 show that when no crack or notch is present the fracture energy is dependent on the radius. This remains true throughout the varying crack depths, despite the overall energy decreasing. The steepness of the curves clearly depends on the radius of the specimen and so Equation 7.1 does not hold true for other radii. The three radii are 0.5, 0.4, and 0.3 cm and their corresponding fracture energies are 500, 310, and 175 J, respectively. The coefficients 1.1, 0.2, and 2.65 for Equation 7.1 are not constant for all specimen radii of a given material since the trend and therefore the coefficients used to describe the trend are radius dependent.

7.3 VARIATION OF FRACTURE ENERGY WITH NOTCH GEOMETRY

The round specimen in Figure 5.2 was given a sharp v-notch 0.1 cm deep with a 30° angle. The notch tip was replaced with a semi-circular root tip of 0.005 cm (viewport 1 of Figure 7.7). The radius of the notch root tip was increased to 0.01 cm then incrementally increased by 0.01 cm. Viewports 2 and 3 of Figure 7.7 show the geometry model for notch

root radii of 0.03 and 0.06 cm, respectively. The notch root radius continued to increase until the notch was completely transformed into a c-notch (viewport 4 of Figure 7.7).

Figure 7.8 shows the fracture energy as the notch geometry transitions from v- to c-notch. As noticed in the previous two sections (7.1 and 7.2), the irradiated case has higher fracture energies than the unirradiated case. Unlike the curves shown in Figures 7.1, 7.5, and 7.6, the unirradiated and irradiated cases follow linear trends. The unirradiated case increases from about 25 J for the notch root radius of 0.01 cm to nearly 40 J for the c-notch. However the irradiated case only increases about 5 J from about 50 to 55 J. Notch geometry has a greater effect on the unirradiated case, which has the steeper slope in Figure 7.8.

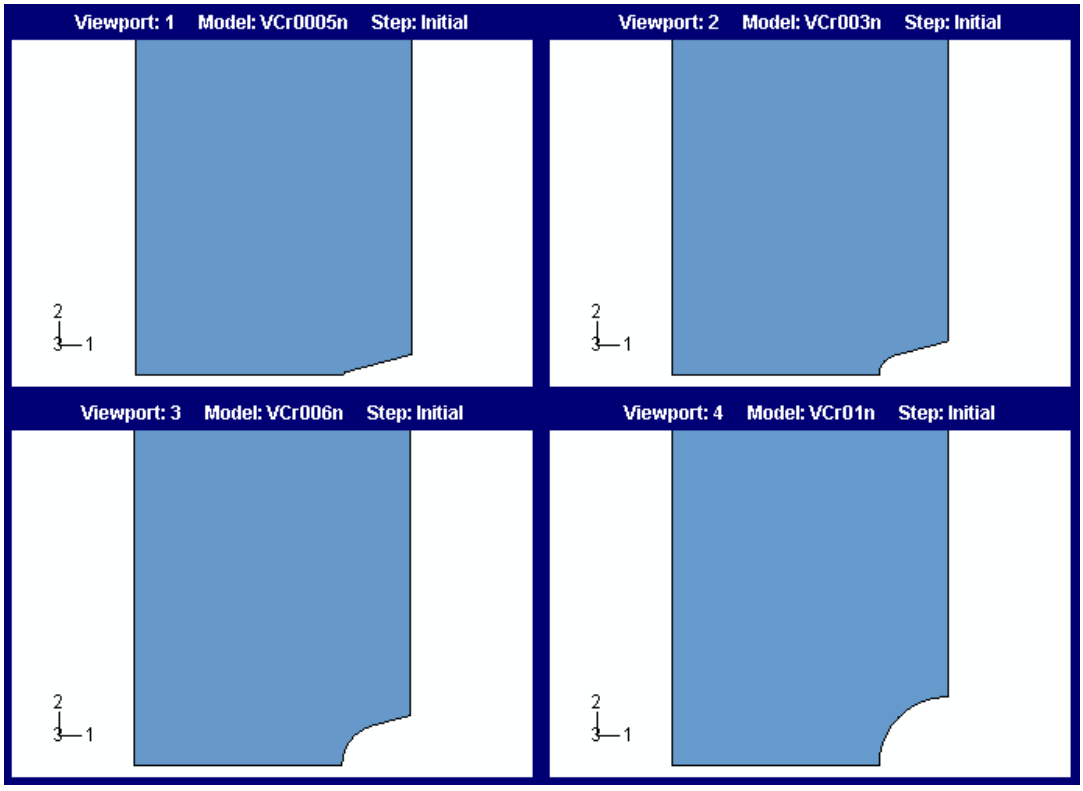

Figure 7.7. Transition of Notch Geometry From V- to C-Notch By Increasing the Notch Root Radius

The trend lines of the unirradiated and irradiated specimens in Figure 7.8 appear as though they would intersect. Projecting these trends further would suggest an intersection at a

notch root radius of 0.25 cm which is beyond the c-notch shape given the depth of the notch is only 0.1 cm. This projection is consistent with the results of the previous two sections. As the notch root radius increases the stress concentration decreases and approaches that of a smooth specimen. When the specimens are smooth the unirradiated case has higher fracture energy.

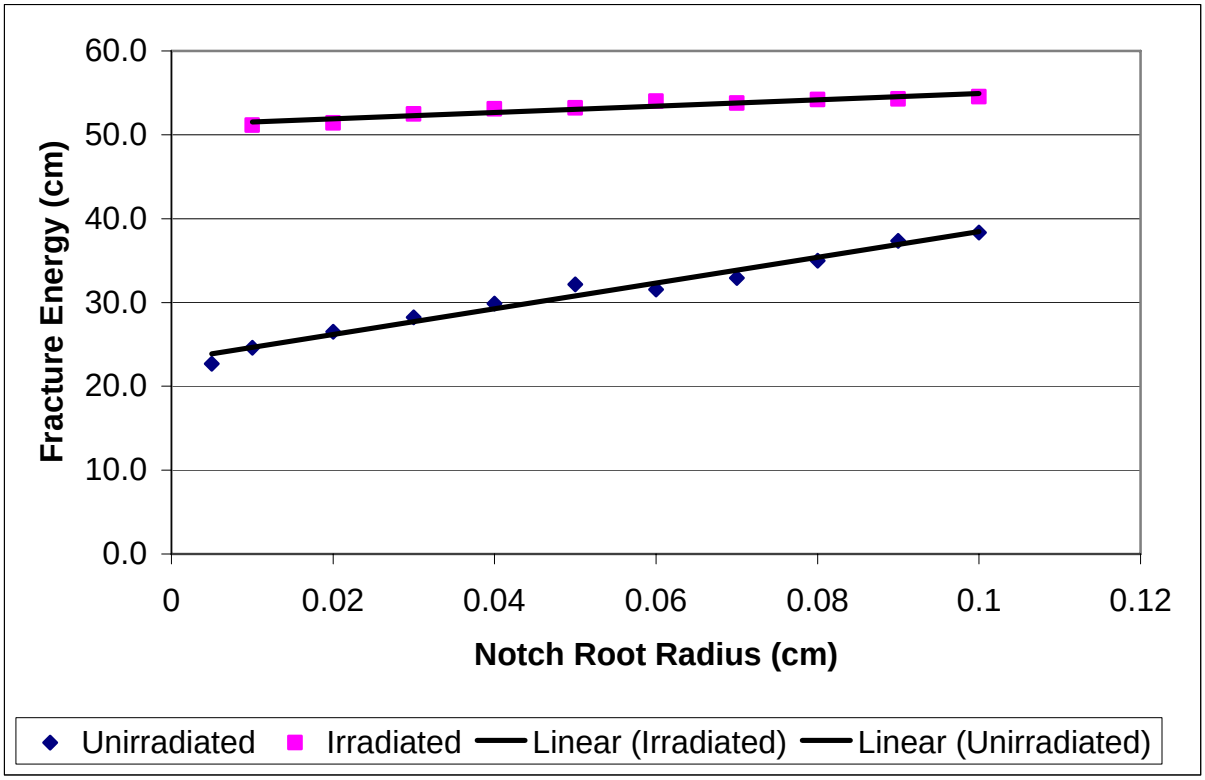

Figure 7.8. Fracture Energy During Transition From V-Notch to C-Notch

The trends of the unirradiated and irradiated specimens are shown in Figures 7.1, and 7.5 intersect. In Figure 7.1, the trends appear to intersect at an angle of 176^{o}. In Figure 7.5, the two trends of the unirradiated and irradiated specimens intersect at a crack depth-to-radius ratio of about 0.05. The intersection of the unirradiated and irradiated specimen trends

in Figures 7.1 and 7.5 mean that the irradiated and unirradiated specimens would have the same fracture energy for certain notch geometries.

The fracture energy of the irradiated specimen consistently exceeds that of the unirradiated specimen in the presence of a reasonably sharp notch (Figures 7.1, 7.5, and 7.8). A probable cause of this phenomenon is due to the differences between the local and global stress and strains. Elements that reach the fracture strain are deleted creating the fracture surface and propagating the crack. Neighboring elements are near the ultimate tensile stress. The global stress-strain for the specimen would be somewhere around the yield stress. Figure 1.3, which appears again as Figure 7.9, illustrates that the ratio of the local to global stress-strain for the irradiated material is less than the unirradiated material. To assist in the understanding of this concept of the local to global ratio, assume the local stress was at the ultimate tensile stress and the global was the yield stress. The irradiated specimen would be less sensitive to the presence of a crack since this ratio is smaller than the unirradiated specimen's ratio. The fracture energy of the specimen would likewise be less sensitive to the presence of a crack and thus would not decrease as much as the unirradiated specimen.

Recall that the fracture energy is the energy under the load-displacement curve, which is proportional to the stress-strain curve. Notice that the global stress for the irradiated specimen would be higher than that of the unirradiated specimen at a given strain. Although the unirradiated specimen has higher strains, the irradiated specimen with its higher stresses could absorb more energy when a crack is present.

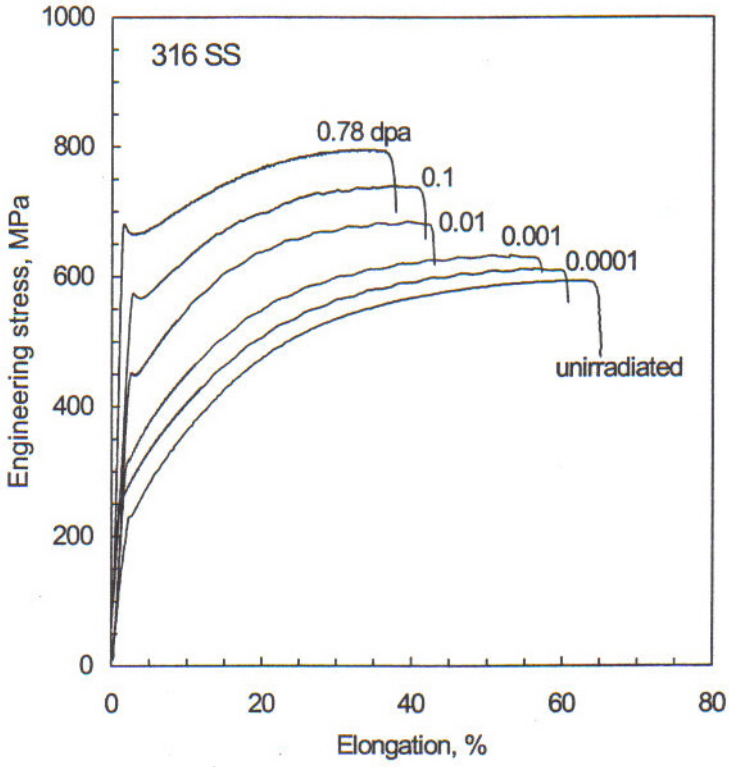

Figure 7.9. Effects of Irradiation on 316 SS [3]

As the irradiated specimen stress concentrators are relaxed and the notched specimen further resembles a smooth specimen, the fracture energy of the irradiated specimen falls below that of the unirradiated specimen. The global stresses and strains are approaching the local ones. At a given notch geometry, the irradiated and unirradiated specimens have the same fracture energy as seen in Figures 7.1 and 7.5 when the unirradiated and irradiated trends intersect. Beyond the intersection, and with the higher global strains, the unirradiated specimen has higher fracture energy.

8. CONCLUSIONS

Finite Element Modeling (FEM) was used to study the effects of flow localization to cracks and notches on fracture energy. The following conclusions were made from this work:

1. Even shallow cracks can reduce the fracture energy substantially, for example, a crack only 0.1 cm deep can reduce the fracture energy in a 0.8 cm diameter round specimen of unirradiated stainless steel 316 from 310 J to about 25 J. This reduction is much higher than a specimen which is reduced in diameter to 0.6 cm (= 0.8 cm - 2 * 0.1 cm) having a fracture energy of 155 J.

2. The fracture energy is practically independent of the crack opening angle for both unirradiated and irradiated specimens for angles less than 140°. Beyond 140° for the unirradiated specimen the fracture energy rises to the fracture energy of a smooth specimen reduced in diameter by two times the crack depth for a round specimen. The relative independence of fracture energy on crack opening angle is due to the fact that as soon as the crack tip propagates the tip is blunted making the effect of the original stress concentration at the crack tip irrelevant.

3. Fracture energy decreases exponentially as the crack depth increases for both unirradiated and irradiated specimens.

4. The fracture energy linearly increases as the notch root radius increases given a constant crack depth for both unirradiated and irradiated specimens.

5. The irradiated specimen fracture energy is less sensitive to the notch root radius than the unirradiated specimen.

6. The fracture energies for the irradiated notched and cracked specimens are generally greater than that of the unirradiated notched and cracked specimens.

7. As the irradiated specimen stress concentrators are relaxed and the notched specimen further resembles a smooth specimen, the fracture energy of the irradiated specimen falls below that of the unirradiated specimen. At a given notch geometry, the irradiated and unirradiated specimens have the same fracture energy.

APPENDIX A

Example ABAQUS Explicit Input

The rectangular bar model used in Section 5.3 for MLHM benchmarking is presented in the following pages as an example of an ABAQUS Explicit input used with the MLHM user subroutine.

```
*Heading
** Job name: Sideners2n Model name: Sideners2n
*Preprint, echo=NO, model=NO, history=NO, contact=NO
**
** PARTS
**
*Part, name=Part-1
*End Part
**
**
** ASSEMBLY
**
*Assembly, name=Assembly
**
*Instance, name=Part-1-1, part=Part-1
*Node
      1,       -10.,       -10.,        200.
      2,       -10.,         0.,        200.
      3,       -10.,        10.,        200.
      4,       -10.,       -10.,        190.
      5,       -10.,         0.,        190.
      6,       -10.,        10.,        190.
      7,       -10.,       -10.,        180.
```

8, -10., 0., 180.

9, -10., 10., 180.

10, -10., -10., 170.

11, -10., 0., 170.

12, -10., 10., 170.

13, -10., -10., 160.

14, -10., 0., 160.

15, -10., 10., 160.

16, -10., -10., 150.

17, -10., 0., 150.

18, -10., 10., 150.

19, -10., -10., 140.

20, -10., 0., 140.

21, -10., 10., 140.

22, -10., -10., 130.

23, -10., 0., 130.

24, -10., 10., 130.

25, -10., -10., 120.

26, -10., 0., 120.

27, -10., 10., 120.

28, -10., -10., 110.

29, -10., 0., 110.

30, -10., 10., 110.

31, -10., -10., 100.

32, -10., 0., 100.

33, -10., 10., 100.

34, -10., -10., 90.

35, -10., 0., 90.

36, -10., 10., 90.

37, -10., -10., 80.

38, -10., 0., 80.

39, -10., 10., 80.

40, -10., -10., 70.

41, -10., 0., 70.

42, -10., 10., 70.

43, -10., -10., 60.

44, -10., 0., 60.

45, -10., 10., 60.

46, -10., -10., 50.

47, -10., 0., 50.

48, -10., 10., 50.

49, -10., -10., 40.

50, -10., 0., 40.

51, -10., 10., 40.

52, -10., -10., 30.

53, -10., 0., 30.

54, -10., 10., 30.

55, -10., -10., 20.

56, -10., 0., 20.

57, -10., 10., 20.

58, -10., -10., 10.

59, -10., 0., 10.

60, -10., 10., 10.

61, -10., -10., 0.

62, -10., 0., 0.

63, -10., 10., 0.

64, 0., -10., 200.

65, 0., 0., 200.

66, 0., 10., 200.

67, 0., -10., 190.

68, 0., 0., 190.

69, 0., 10., 190.

70, 0., -10., 180.

71, 0., 0., 180.

72, 0., 10., 180.

73, 0., -10., 170.

74, 0., 0., 170.

75, 0., 10., 170.

76, 0., -10., 160.

77, 0., 0., 160.

78, 0., 10., 160.

79, 0., -10., 150.

80, 0., 0., 150.

81, 0., 10., 150.

82, 0., -10., 140.

83, 0., 0., 140.

84, 0., 10., 140.

85, 0., -10., 130.

86, 0., 0., 130.

87, 0., 10., 130.

88, 0., -10., 120.

89, 0., 0., 120.

90, 0., 10., 120.

91, 0., -10., 110.

92, 0., 0., 110.

93, 0., 10., 110.

94, 0., -10., 100.

95, 0., 0., 100.

96, 0., 10., 100.

97, 0., -10., 90.

98, 0., 0., 90.

99, 0., 10., 90.

100, 0., -10., 80.

101, 0., 0., 80.

102, 0., 10., 80.

103, 0., -10., 70.

104, 0., 0., 70.

105, 0., 10., 70.

106, 0., -10., 60.

107, 0., 0., 60.

108, 0., 10., 60.

109, 0., -10., 50.

110, 0., 0., 50.

111, 0., 10., 50.

112, 0., -10., 40.

113, 0., 0., 40.

114, 0., 10., 40.

115, 0., -10., 30.

116, 0., 0., 30.

117, 0., 10., 30.

118, 0., -10., 20.

119, 0., 0., 20.

120, 0., 10., 20.

121, 0., -10., 10.

122, 0., 0., 10.

123, 0., 10., 10.

124, 0., -10., 0.

125, 0., 0., 0.

126, 0., 10., 0.

127, 10., -10., 200.

128, 10., 0., 200.

129, 10., 10., 200.

130, 10., -10., 190.

131, 10., 0., 190.

132, 10., 10., 190.

133, 10., -10., 180.

134, 10., 0., 180.

135, 10., 10., 180.

136, 10., -10., 170.

137, 10., 0., 170.

138, 10., 10., 170.

139, 10., -10., 160.

140, 10., 0., 160.

141, 10., 10., 160.

142, 10., -10., 150.

143, 10., 0., 150.

144, 10., 10., 150.

145, 10., -10., 140.

146, 10., 0., 140.

147, 10., 10., 140.

148, 10., -10., 130.

149, 10., 0., 130.

150, 10., 10., 130.

151, 10., -10., 120.

152, 10., 0., 120.

153, 10., 10., 120.

154, 10., -10., 110.

155, 10., 0., 110.

156, 10., 10., 110.

157, 10., -10., 100.

158, 10., 0., 100.

159, 10., 10., 100.

160, 10., -10., 90.

161, 10., 0., 90.

162, 10., 10., 90.

163, 10., -10., 80.

164, 10., 0., 80.

165, 10., 10., 80.

166, 10., -10., 70.

167, 10., 0., 70.

168, 10., 10., 70.

169, 10., -10., 60.

170, 10., 0., 60.

171, 10., 10., 60.

172, 10., -10., 50.

173, 10., 0., 50.

174, 10., 10., 50.

175, 10., -10., 40.

176, 10., 0., 40.

177, 10., 10., 40.

178, 10., -10., 30.

179, 10., 0., 30.

180, 10., 10., 30.

181, 10., -10., 20.

182, 10., 0., 20.

183, 10., 10., 20.

184, 10., -10., 10.

185, 10., 0., 10.

186, 10., 10., 10.

187, 10., -10., 0.

188, 10., 0., 0.

189, 10., 10., 0.

*Element, type=C3D8R

1, 64, 65, 68, 67, 1, 2, 5, 4

2, 65, 66, 69, 68, 2, 3, 6, 5

3, 67, 68, 71, 70, 4, 5, 8, 7

4, 68, 69, 72, 71, 5, 6, 9, 8

5, 70, 71, 74, 73, 7, 8, 11, 10

6, 71, 72, 75, 74, 8, 9, 12, 11

7, 73, 74, 77, 76, 10, 11, 14, 13

8, 74, 75, 78, 77, 11, 12, 15, 14

9, 76, 77, 80, 79, 13, 14, 17, 16

10, 77, 78, 81, 80, 14, 15, 18, 17

11, 79, 80, 83, 82, 16, 17, 20, 19

12, 80, 81, 84, 83, 17, 18, 21, 20

13, 82, 83, 86, 85, 19, 20, 23, 22

14, 83, 84, 87, 86, 20, 21, 24, 23

15, 85, 86, 89, 88, 22, 23, 26, 25

16, 86, 87, 90, 89, 23, 24, 27, 26

17, 88, 89, 92, 91, 25, 26, 29, 28

18, 89, 90, 93, 92, 26, 27, 30, 29

19, 91, 92, 95, 94, 28, 29, 32, 31

20, 92, 93, 96, 95, 29, 30, 33, 32

21, 94, 95, 98, 97, 31, 32, 35, 34

22, 95, 96, 99, 98, 32, 33, 36, 35

23, 97, 98, 101, 100, 34, 35, 38, 37

24, 98, 99, 102, 101, 35, 36, 39, 38

25, 100, 101, 104, 103, 37, 38, 41, 40

26, 101, 102, 105, 104, 38, 39, 42, 41

27, 103, 104, 107, 106, 40, 41, 44, 43

28, 104, 105, 108, 107, 41, 42, 45, 44

29, 106, 107, 110, 109, 43, 44, 47, 46

30, 107, 108, 111, 110, 44, 45, 48, 47

31, 109, 110, 113, 112, 46, 47, 50, 49

32, 110, 111, 114, 113, 47, 48, 51, 50

33, 112, 113, 116, 115, 49, 50, 53, 52

34, 113, 114, 117, 116, 50, 51, 54, 53

35, 115, 116, 119, 118, 52, 53, 56, 55

36, 116, 117, 120, 119, 53, 54, 57, 56

37, 118, 119, 122, 121, 55, 56, 59, 58

38, 119, 120, 123, 122, 56, 57, 60, 59

39, 121, 122, 125, 124, 58, 59, 62, 61

40, 122, 123, 126, 125, 59, 60, 63, 62

41, 127, 128, 131, 130, 64, 65, 68, 67

42, 128, 129, 132, 131, 65, 66, 69, 68

43, 130, 131, 134, 133, 67, 68, 71, 70

44, 131, 132, 135, 134, 68, 69, 72, 71

45, 133, 134, 137, 136, 70, 71, 74, 73

46, 134, 135, 138, 137, 71, 72, 75, 74

47, 136, 137, 140, 139, 73, 74, 77, 76

48, 137, 138, 141, 140, 74, 75, 78, 77

49, 139, 140, 143, 142, 76, 77, 80, 79

50, 140, 141, 144, 143, 77, 78, 81, 80

51, 142, 143, 146, 145, 79, 80, 83, 82

52, 143, 144, 147, 146, 80, 81, 84, 83

53, 145, 146, 149, 148, 82, 83, 86, 85

54, 146, 147, 150, 149, 83, 84, 87, 86

55, 148, 149, 152, 151, 85, 86, 89, 88

56, 149, 150, 153, 152, 86, 87, 90, 89

57, 151, 152, 155, 154, 88, 89, 92, 91

58, 152, 153, 156, 155, 89, 90, 93, 92

59, 154, 155, 158, 157, 91, 92, 95, 94

60, 155, 156, 159, 158, 92, 93, 96, 95

61, 157, 158, 161, 160, 94, 95, 98, 97

62, 158, 159, 162, 161, 95, 96, 99, 98

63, 160, 161, 164, 163, 97, 98, 101, 100

64, 161, 162, 165, 164, 98, 99, 102, 101

65, 163, 164, 167, 166, 100, 101, 104, 103

66, 164, 165, 168, 167, 101, 102, 105, 104

67, 166, 167, 170, 169, 103, 104, 107, 106

68, 167, 168, 171, 170, 104, 105, 108, 107

69, 169, 170, 173, 172, 106, 107, 110, 109

70, 170, 171, 174, 173, 107, 108, 111, 110

71, 172, 173, 176, 175, 109, 110, 113, 112

72, 173, 174, 177, 176, 110, 111, 114, 113

73, 175, 176, 179, 178, 112, 113, 116, 115

74, 176, 177, 180, 179, 113, 114, 117, 116

75, 178, 179, 182, 181, 115, 116, 119, 118

76, 179, 180, 183, 182, 116, 117, 120, 119

77, 181, 182, 185, 184, 118, 119, 122, 121

78, 182, 183, 186, 185, 119, 120, 123, 122

79, 184, 185, 188, 187, 121, 122, 125, 124

80, 185, 186, 189, 188, 122, 123, 126, 125

*Nset, nset=_PickedSet2, internal, generate

 1, 189, 1

*Elset, elset=_PickedSet2, internal, generate

 1, 80, 1

** Region: (Section-1:Picked)

*Elset, elset=_PickedSet2, internal, generate

 1, 80, 1

** Section: Section-1

*Solid Section, elset=_PickedSet2, material=Material-1

1.,

*End Instance

**

*Nset, nset=_PickedSet8, internal, instance=Part-1-1

 1, 2, 3, 64, 65, 66, 127, 128, 129

*Elset, elset=_PickedSet8, internal, instance=Part-1-1

 1, 2, 41, 42

*Nset, nset=_PickedSet9, internal, instance=Part-1-1

```
 61,  62,  63, 124, 125, 126, 187, 188, 189
*Elset, elset=_PickedSet9, internal, instance=Part-1-1
 39, 40, 79, 80
*Nset, nset=Set-1, instance=Part-1-1, generate
   1,  189,    1
*Elset, elset=Set-1, instance=Part-1-1, generate
  1,  80,   1
*End Assembly
**
** MATERIALS
**
*Material, name=Material-1
*Density
 7.99,
*Depvar, delete=2
      3,
*User Material, constants=10
 1.93e+12,        0.3,    0.415628,    0.515628,    2.84e+09, 2.65413e+10,   0.0413818, 1.59454e+10
    0.206128, 1.15361e+10
** ----------------------------------------------------------------
**
** STEP: Step-1
**
*Step, name=Step-1
*Dynamic, Explicit
, 20.
*Bulk Viscosity
0.06, 1.2
```

```
**
** BOUNDARY CONDITIONS
**
** Name: BC-4 Type: Velocity/Angular velocity
*Boundary, type=VELOCITY
_PickedSet8, 3, 3, 0.5
** Name: BC-5 Type: Velocity/Angular velocity
*Boundary, type=VELOCITY
_PickedSet9, 3, 3, -0.5
**
** OUTPUT REQUESTS
**
*Restart, write, number interval=1, time marks=NO
**
** FIELD OUTPUT: F-Output-1
**
*Output, field
*Node Output
A, RF, U, V
*Element Output, directions=YES
E, ELEDEN, ELEN, ENER, LE, NE, PE, PEEQ, S, SDEG, STATUS
*Contact Output
CSTRESS,
**
** HISTORY OUTPUT: H-Output-1
**
*Output, history, frequency=250
*Element Output, elset=Set-1
```

E33, MISES, NE33, S11, S22, S33

*Energy Output, elset=Set-1

ALLAE, ALLCD, ALLDMD, ALLFD, ALLIE, ALLKE, ALLPD, ALLSE, ALLVD, ALLWK,

ETOTAL

**

** HISTORY OUTPUT: H-Output-2

**

*Output, history, variable=PRESELECT

*End Step

** --

**

** STEP: Step-2

**

*Step, name=Step-2

*Dynamic, Explicit

, 20.

*Bulk Viscosity

0.06, 1.2

**

** OUTPUT REQUESTS

**

*Restart, write, number interval=1, time marks=NO

**

** FIELD OUTPUT: F-Output-1

**

*Output, field

*Node Output

A, RF, U, V

*Element Output, directions=YES

E, ELEDEN, ELEN, ENER, LE, NE, PE, PEEQ, S, SDEG, STATUS

*Contact Output

CSTRESS,

**

** HISTORY OUTPUT: H-Output-1

**

*Output, history, frequency=250

*Element Output, elset=Set-1

E33, MISES, NE33, S11, S22, S33

*Energy Output, elset=Set-1

ALLAE, ALLCD, ALLDMD, ALLFD, ALLIE, ALLKE, ALLPD, ALLSE, ALLVD, ALLWK,

ETOTAL

**

** HISTORY OUTPUT: H-Output-2

**

*Output, history, variable=PRESELECT

*End Step

** --

**

** STEP: Step-3

**

*Step, name=Step-3

*Dynamic, Explicit

, 20.

*Bulk Viscosity

0.06, 1.2

**

```
** OUTPUT REQUESTS
**
*Restart, write, number interval=1, time marks=NO
**
** FIELD OUTPUT: F-Output-1
**
*Output, field
*Node Output
A, RF, U, V
*Element Output, directions=YES
E, ELEDEN, ELEN, ENER, LE, NE, PE, PEEQ, S, SDEG, STATUS
*Contact Output
CSTRESS,
**
** HISTORY OUTPUT: H-Output-1
**
*Output, history, frequency=250
*Element Output, elset=Set-1
E33, MISES, NE33, S11, S22, S33
*Energy Output, elset=Set-1
ALLAE, ALLCD, ALLDMD, ALLFD, ALLIE, ALLKE, ALLPD, ALLSE, ALLVD, ALLWK,
ETOTAL
**
** HISTORY OUTPUT: H-Output-2
**
*Output, history, variable=PRESELECT
*End Step
** ----------------------------------------------------------------
```

```
**
** STEP: Step-4
**
*Step, name=Step-4
*Dynamic, Explicit
, 20.
*Bulk Viscosity
0.06, 1.2
**
** OUTPUT REQUESTS
**
*Restart, write, number interval=1, time marks=NO
**
** FIELD OUTPUT: F-Output-1
**
*Output, field
*Node Output
A, RF, U, V
*Element Output, directions=YES
E, ELEDEN, ELEN, ENER, LE, NE, PE, PEEQ, S, SDEG, STATUS
*Contact Output
CSTRESS,
**
** HISTORY OUTPUT: H-Output-1
**
*Output, history, frequency=250
*Element Output, elset=Set-1
E33, MISES, NE33, S11, S22, S33
```

```
*Energy Output, elset=Set-1
ALLAE, ALLCD, ALLDMD, ALLFD, ALLIE, ALLKE, ALLPD, ALLSE, ALLVD, ALLWK,
ETOTAL
**
** HISTORY OUTPUT: H-Output-2
**
*Output, history, variable=PRESELECT
*End Step
** ----------------------------------------------------------------
**
** STEP: Step-5
**
*Step, name=Step-5
*Dynamic, Explicit
, 20.
*Bulk Viscosity
0.06, 1.2
**
** OUTPUT REQUESTS
**
*Restart, write, number interval=1, time marks=NO
**
** FIELD OUTPUT: F-Output-1
**
*Output, field
*Node Output
A, RF, U, V
*Element Output, directions=YES
```

E, ELEDEN, ELEN, ENER, LE, NE, PE, PEEQ, S, SDEG, STATUS

*Contact Output

CSTRESS,

**

** HISTORY OUTPUT: H-Output-1

**

*Output, history, frequency=250

*Element Output, elset=Set-1

E33, MISES, NE33, S11, S22, S33

*Energy Output, elset=Set-1

ALLAE, ALLCD, ALLDMD, ALLFD, ALLIE, ALLKE, ALLPD, ALLSE, ALLVD, ALLWK,

ETOTAL

**

** HISTORY OUTPUT: H-Output-2

**

*Output, history, variable=PRESELECT

*End Step

** --

**

** STEP: Step-6

**

*Step, name=Step-6

*Dynamic, Explicit

, 20.

*Bulk Viscosity

0.06, 1.2

**

** OUTPUT REQUESTS

```
**
*Restart, write, number interval=1, time marks=NO
**
** FIELD OUTPUT: F-Output-1
**
*Output, field
*Node Output
A, RF, U, V
*Element Output, directions=YES
E, ELEDEN, ELEN, ENER, LE, NE, PE, PEEQ, S, SDEG, STATUS
*Contact Output
CSTRESS,
**
** HISTORY OUTPUT: H-Output-1
**
*Output, history, frequency=1000
*Element Output, elset=Set-1
E33, MISES, NE33, S11, S22, S33
*Energy Output, elset=Set-1
ALLAE, ALLCD, ALLDMD, ALLFD, ALLIE, ALLKE, ALLPD, ALLSE, ALLVD, ALLWK,
ETOTAL
**
** HISTORY OUTPUT: H-Output-2
**
*Output, history, variable=PRESELECT
*End Step
** ----------------------------------------------------------------
**
```

```
** STEP: Step-7
**
*Step, name=Step-7
*Dynamic, Explicit
, 20.
*Bulk Viscosity
0.06, 1.2
**
** OUTPUT REQUESTS
**
*Restart, write, number interval=1, time marks=NO
**
** FIELD OUTPUT: F-Output-1
**
*Output, field
*Node Output
A, RF, U, V
*Element Output, directions=YES
E, ELEDEN, ELEN, ENER, LE, NE, PE, PEEQ, S, SDEG, STATUS
*Contact Output
CSTRESS,
**
** HISTORY OUTPUT: H-Output-1
**
*Output, history, frequency=1000
*Element Output, elset=Set-1
E33, MISES, NE33, S11, S22, S33
*Energy Output, elset=Set-1
```

ALLAE, ALLCD, ALLDMD, ALLFD, ALLIE, ALLKE, ALLPD, ALLSE, ALLVD, ALLWK,

ETOTAL

**

** HISTORY OUTPUT: H-Output-2

**

*Output, history, variable=PRESELECT

*End Step

** --

**

** STEP: Step-8

**

*Step, name=Step-8

*Dynamic, Explicit

, 10.

*Bulk Viscosity

0.06, 1.2

**

** OUTPUT REQUESTS

**

*Restart, write, number interval=1, time marks=NO

**

** FIELD OUTPUT: F-Output-1

**

*Output, field, number interval=10

*Node Output

A, RF, U, V

*Element Output, directions=YES

E, ELEDEN, ELEN, ENER, LE, NE, PE, PEEQ, S, SDEG, STATUS

*Contact Output

CSTRESS,

**

** HISTORY OUTPUT: H-Output-1

**

*Output, history, frequency=1000

*Element Output, elset=Set-1

E33, MISES, NE33, S11, S22, S33

*Energy Output, elset=Set-1

ALLAE, ALLCD, ALLDMD, ALLFD, ALLIE, ALLKE, ALLPD, ALLSE, ALLVD, ALLWK,

ETOTAL

**

** HISTORY OUTPUT: H-Output-2

**

*Output, history, variable=PRESELECT

*End Step

APPENDIX B

2D ABAQUS Explicit Execution Script

A multitude of simulations were conducted using ABAQUS Explicit and the MLHM user subroutine. A pearl script was written to execute the simulations automatically from a list of input files. The script was inspired by another script used for MCNP simulation executions. The MCNP script was developed by Brandon Distler and Victor Smith. The ABAQUS Explicit Execution Script is present on the following pages.

```
#!perl
use File::Copy;
$abaqusstuff = "user=mlf2d cpus=4 parallel=domain domains=4 mp_mode=threads
memory=8000000000 interactive double";
print "\n";
$doublecheck = 1;
open (LIST, "<arml2D.txt")|| die "Cannot open arml2D.txt: $!";
MAGIC: while ($line = <LIST>) {
 if ($line =~ m|(.*n)$|) {
  chomp ($cur = $1);
  if (open (OUT, "<${cur}.odb")) {
   close OUT;
   if (open (LOCK, "<${cur}.lck")) {
    close LOCK;
    system "del ${cur}.lck";
    system "del ${cur}.log";
    system "del ${cur}batch.bat";
    open (BATCH, ">${cur}batch.bat");
    print BATCH "abaqus job=$cur recover input=$cur $abaqusstuff";
    close BATCH;
```

```
  print "Recovering and Resuming $cur\n";
  $doublecheck = 0;
  system "${cur}batch.bat";
 } elsif (open(OUTF, "<${cur}.odb_f")) {
  close OUTF;
  open (REPORT, ">abaqusbad${cur}");
  print REPORT "$cur Failed to run properly!  See ${cur}.dat or ${cur}.sta or ${cur}.msg.";
  close REPORT;
  print "$cur failed to run properly.\n";
 } else {
  print "$cur has already been completed!\n";
  if (open(ABQ, "<${cur}.abq")) {
   close ABQ;
   system "del ${cur}.abq ${cur}.com ${cur}.dat ${cur}.mdl ${cur}.msg";
   system "del ${cur}.pac ${cur}.prt ${cur}.res ${cur}.sel";
   system "del ${cur}.stt ${cur}batch.bat";
  };
  goto MAGIC;
 };
} else {
 if (open (INP, "<${cur}.inp")) {
  close INP;
  open (BATCH, ">${cur}batch.bat");
  print BATCH "abaqus job=$cur analysis input=$cur $abaqusstuff output_precision=full";
  close BATCH;
  $doublecheck = 0;
  system "${cur}batch.bat";
 } else {
```

```
    print "Cannot open ${cur}.inp: $!\n";
   };
  };
} elsif ($line =~ m|(.*c)$|) {
  chomp ($cur = $1);
  if (open (OUT, "<${cur}.odb")) {
   close OUT;
   if (open (LOCK, "<${cur}.lck")) {
    close LOCK;
    system "del ${cur}.lck";
    system "del ${cur}.log";
    system "del ${cur}batch.bat";
    open (BATCH, ">${cur}batch.bat");
    print BATCH "abaqus job=$cur recover input=$cur $abaqusstuff";
    close BATCH;
    print "Recovering and Resuming $cur\n";
    $doublecheck = 0;
    system "${cur}batch.bat";
   } elsif (open(OUTF, "<${cur}.odb_f")) {
    close OUTF;
    open (REPORT, ">abaqusbad${cur}");
    print REPORT "$cur Failed to run properly!  See ${cur}.dat or ${cur}.sta or ${cur}.msg.";
    close REPORT;
    print "$cur failed to run properly.\n";
   } else {
    print "$cur has already been completed!\n";
    if (open(ABQ, "<${cur}.abq")) {
     close ABQ;
```

```
        system "del ${cur}.abq ${cur}.com ${cur}.dat ${cur}.mdl ${cur}.msg";
        system "del ${cur}.pac ${cur}.prt ${cur}.res ${cur}.sel";
        system "del ${cur}.stt ${cur}batch.bat";
       };
       goto MAGIC;
     };
    } else {
     if (open (INP, "<${cur}.inp")) {
       chop $cur if ($cur =~ /.*c$/);
       $old = $cur;
       $cur = $cur."c";
       open (BATCH, ">${cur}batch.bat");
       print BATCH "abaqus job=$cur oldjob=$old input=$cur $abaqusstuff output_precision=full";
       close BATCH;
       $doublecheck = 0;
       system "${cur}batch.bat";
     } else {
       print "Cannot open ${cur}.inp: $!\n";
     };
    };
  };
};
close LIST;
if ($doublecheck==0) {
  close LIST;
  $doublecheck=$doublecheck+1;
  open (LIST, "<arml2D.txt")|| die "Cannot open arml2D.txt for double checking: $!";
  print "\nDouble checking the list...\n\n";
```

```
  goto MAGIC;
};
print "\n";
print "All available files on the list have been run to completion!\n";
print "(Unless they did not run properly.)\n";
```

REFERENCES

[1] Anderson, T. L. Fracture Mechanics: Fundamentals and Applications. Third Edition. Boca Ratan, FL. CRC Press. 2005.

[2] Scott, P. M., Meunier, M.-C., Deydier, D., Silvestre, S. , and Trenty, A., "An Analysis of Baffle/Former Bolt Cracking French PWRs," Environmentally Assisted Cracking: Predictive Methods for Risk Assessment and Evaluation of Materials, Equipment, and Structures, ASTM 1401, R. D. Kane, Ed., American Society for Testing and Materials, West Conshohocken, PA, 2000.

[3] Farrell, K., Byun, T. S., and Hashimoto, N. Mapping Flow Localization Processes in Deformation of Irradiated Reactor Structural Alloys. ORNL/TM-2002/66. July 2002.

[4] Fish, Robert L. "Notch Effect on the Tensile Properties of Fast-Reactor-Irradiated Type 304 Stainless Steel", Nuclear Technology. 31. October 1976. pp. 85-95.

[5] Sidener, S. E., et. al. "Dynamic finite element modeling of the effects of size on the upper self energy of pressure vessel steels", International Symposia on Advanced Materials and Technology for the 21st Century. Honolulu, Hawaii. Decemeber 13-15, 1995.

[6] Kumar, A. S., Sidener, S. E., and Hamilton, M. L., "Dynamic finite element modeling of the upper self energy of precracked charpy specimens of neutron irradiated weld metal 72W", Effects of Radiation on Materials: 18th International Symposium, ASTM STP 1324. R. K. Nanstad, M. L. Hamilton, F. A. Garner, and A. S. Kumar, Eds., American Society for Testing and Materials, 1997.

[7] McCoy, J. H., Kumar, A. S., and Stubbins, J. F. "Deformation and fracture of Cu alloy-stainless steel layered structures under dynamic loading", " Journal of Nuclear Materials. 258-263. 1998. 1033-1039.

[8] McCoy, J. H., Kumar, A. S., and Stubbins, J. F. "Effects of interface and tensile properties in the dynamic fracture of layered structures" Journal of Nuclear Materials. 270. 1999. pp. 129-133.

[9] McCoy, J. H. and Kumar, A. S., "Dynamic Finite Element Modeling of Fracture in Charpy V-Notch Specimens of Weld Material 72W", Journal of ASTM International, Vol. 3. No. 5. Paper ID JAI12451. 2006.

[10] Kim, Yun-Jae, "Fully plastic analyses for notched bars and plates using finite element limit analysis", Engineering Fracture Mechanics. 73. 2006. 1849-1864.

[11] Wu, X., Pan, X., and Stubbins J. F. "Analysis of notch strengthening of 316L stainless steel with and without irradiation-induced hardening using EBSD and FEM", Journal of Nuclear Materials. 361. 2007. pp. 228-238.

[12] ABAQUS Analysis User's Manual, Version 6.6 Documentation, Simulia, 2006.

[13] ABAQUS CAE Manual, Version 6.6 Documentation, Simulia, 2006.

[14] ABAQUS Theory Manual, Version 6.6 Documentation, Simulia, 2006.

[15] McCoy, Jaime H. Dynamic Finite Element Analysis of Precracked, Notched, and Layered Charpy Impact Tests. Dissertation. University of Missouri – Rolla. 2003.

[16] ABAQUS Verification Manual, Version 6.6 Documentation, Simulia, 2006.

[17] Getting Started Manual, Version 7.5, OriginLab Corporation, 2003.

[18] Maloy, S. A., et. al. "The mechanical properties of 316L/304L stainless steels, Alloy 718 and Mod 9Cr-1Mo after irradiation in a spallation environment", Journal of Nuclear Materials. 296. 2001. pp. 119-128.